J. Fluid Mech. (2014), *vol.* 755, *pp.* 142–175. © Cambridge University Press 2014
doi:10.1017/jfm.2014.394

Modelling of material pitting from cavitation bubble collapse

Chao-Tsung Hsiao†, A. Jayaprakash, A. Kapahi, J.-K. Choi and Georges L. Chahine

DYNAFLOW, INC., 10621-J Iron Bridge Road, Jessup, MD 20794, USA

(Received 23 December 2013; revised 16 June 2014; accepted 3 July 2014;
first published online 14 August 2014)

Material pitting from cavitation bubble collapse is investigated numerically including two-way fluid–structure interaction (FSI). A hybrid numerical approach which links an incompressible boundary element method (BEM) solver and a compressible finite difference flow solver is applied to capture non-spherical bubble dynamics efficiently and accurately. The flow codes solve the fluid dynamics while intimately coupling the solution with a finite element structure code to enable simulation of the full FSI. During bubble collapse high impulsive pressures result from the impact of the bubble re-entrant jet on the material surface and from the collapse of the remaining bubble ring. A pit forms on the material surface when the impulsive pressure is large enough to result in high equivalent stresses exceeding the material yield stress. The results depend on bubble dynamics parameters such as the size of the bubble at its maximum volume, the bubble standoff distance from the material wall, and the pressure driving the bubble collapse. The effects of these parameters on the re-entrant jet, the following bubble ring collapse pressure, and the generated material pit characteristics are investigated.

Key words: bubble dynamics, cavitation, shock waves

1. Introduction

Cavitation erosion in rotating machinery such as pumps, impellers, propellers, etc. is a main concern for the marine, pump, and other industries. Cavitation is due to the high relative motion between the liquid and the subject lifting surface. As a result of the high velocities, the local pressure in the liquid drops below a critical pressure (e.g. the liquid vapour pressure) and this drives nuclei (microbubbles always present in liquids) to grow explosively. When the pressure returns to a high value along the path of these bubbles, volume implosions occur and this can generate high-pressure pulses and shock waves (Rayleigh 1917). Many pioneering studies (Naude & Ellis 1961; Plesset & Chapman 1971; Crum 1979; Chahine 1982) have shown, experimentally as well as analytically, that the collapse of these cavitation bubbles near a rigid boundary also results in high-speed re-entrant liquid jets, which penetrate the highly deformed bubbles and strike the nearby boundary generating water hammer like impact pressures. Both shock waves and high-speed re-entrant liquid jets produce

† Email address for correspondence: ctsung@dynaflow-inc.com

https://doi.org/10.1017/jfm.2014.394 Published online by Cambridge University Press

high local stresses on the adjacent material surface and are responsible for material micro-deformations and damage.

While a 'weak' material may fail rapidly under the repeated shock waves and liquid jet impacts, a resistant material actually experiences the symptoms of fatigue. Initially the material surface gets deformed and is modified microscopically without any loss of material. This is accompanied by work hardening of the surface. During this initial phase called incubation period, permanent deformation occurs accompanied by plastic and local displacement of material micro-particles as well as with development of micro-cracks in brittle materials. The pits formed on the material surface during the incubation period are good indicators of the material strength, although advanced damage to the material, resulting in weight loss and fracture, occurs at a later stage of the cavitation erosion process (Kim *et al.* 2014).

Since the formation of a pit on the material surface is reasonably associated with a single cavitation event caused by bubble collapse, the amount of permanent deformation should depend on the stresses the collapsing bubble creates on the material. It is thus expected that the formation of material pitting can be simulated using a fluid–structure interaction model of the dynamics of the bubbles (single bubble or clouds of bubble) and the material concerned. Simulation of the collapse of a bubble near a rigid wall has been an active research area since the pioneering work of Plesset & Chapman (1971). The resulting re-entrant jet has been found to play an important role in hydrodynamics and ultrasonic cavitation, as well as in large-scale underwater explosion problems (Chahine & Perdue 1990; Kalumuck, Chahine & Hsiao 2003; Jayaprakash, Hsiao & Chahine 2012) and in small-scale medical applications (Hsiao & Chahine 2013*b*).

It is known that the formation of the re-entrant jet and the resultant pressures are highly dependent on the standoff distance, i.e. the distance between the initial bubble centre and the wall (Chahine 1982; Blake & Gibson 1987; Zhang, Duncan & Chahine 1993; Wardlaw & Luton 2000). Classically the numerical simulations start from the bubble being spherical and at its maximum radius. The bubble is then allowed to collapse in response to the high ambient pressure. Such an approach is not suitable for studying cavitation bubbles growing very close to the boundary. For these small standoff distances scenarios (standoff less than one bubble radius) the impact pressures due to the re-entrant jet have been computed numerically (Chahine, Duraiswami & Kalumuck 1996; Chahine *et al.* 2006; Jayaprakash *et al.* 2012) and measured experimentally (Vogel & Lauterborn 1988; Philipp & Lauterborn 1998; Harris *et al.* 2009) to attain a maximum at distances of the order of three-quarters of the maximum bubble radius. Therefore, simulations of the bubble dynamics starting from a small nucleus are necessary to cover a more complete range of standoff distances to understand such effects on the material pitting.

Since both the impact of a high-speed liquid jet on the wall and bubble collapse will generate local high-pressure waves, a compressible flow solver is desired to capture accurately pressure waves and any shock wave emission and propagation. However, such flow solvers usually use a finite difference method which requires very fine spatial resolution and small time step sizes especially for resolving the formation of the re-entrant jet accurately (Wardlaw & Luton 2000). This makes them not very efficient for simulating the relatively long duration bubble period. To overcome this, a hybrid numerical procedure combining an incompressible solver and a compressible code is applied here to capture both the full period of the bubble dynamics as well as the shock phases occurring at initiation for an explosion bubble and during bubble collapse and rebound for both cavitation and underwater explosion

https://doi.org/10.1017/jfm.2014.394 Published online by Cambridge University Press

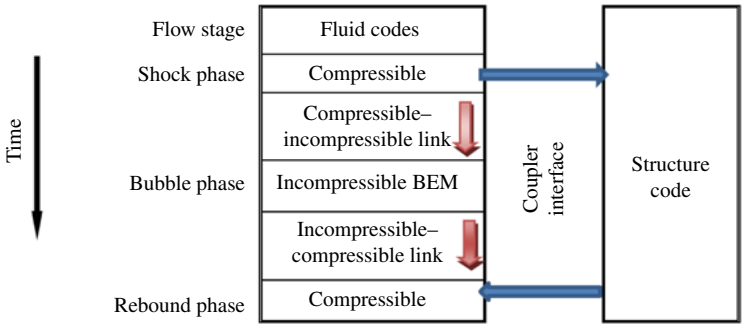


FIGURE 1. (Colour online) Schematic diagram of the numerical approach used to simulate the interaction between a highly inertial bubble or a cavitation bubble and a structure.

bubbles. This numerical procedure takes advantage of an accurate shock capturing method and of a boundary element method (BEM) both shown to be very efficient in modelling underwater explosion and cavitation bubble dynamics problems and very accurate in capturing the re-entrant jet.

As already shown by previous studies (Duncan, Milligan & Zhange 1991; Duncan, Milligan & Zhang 1996; Wardlaw & Luton 2000; Madadi-Kandjani & Xiong 2014), the deformable wall can alter bubble dynamics during collapse. Therefore, simulation of both fluid and material responses and their interaction is required to model accurately material pitting due to bubble collapse. Both the impact of the high-speed re-entrant liquid jet on the wall and the emission and propagation of shock waves from the bubble collapse require a compressible flow solver. In this study, a finite element structure code is coupled with such a compressible flow solver to investigate the material response to the pressure field generated by the bubble dynamics. In the case of highly deformable materials the motion of the material interface also affects the bubble dynamics. This paper aims at isolating the influence of the various physical parameters such as the pressure driving the bubble collapse, the bubble size, the bubble distance from the wall, and the properties of the damaged material.

2. Numerical approach

The numerical approach applied to model material pitting in this paper is part of a general hybrid approach which was developed by the authors to simulate fluid structure interaction (FSI) problems involving shock and bubble pressure pulses (Hsiao & Chahine 2013*a*) As illustrated in figure 1, for a highly inertial bubble such as underwater explosion bubble (UNDEX) or a laser-generated bubble (Philipp & Lauterborn 1998; Vogel & Lauterborn 1988) a compressible–incompressible link is required at the beginning to handle the emitted shock wave and the flow field generated by the exploding bubble. Cavitation bubbles on the other hand, generate a small pressure peak and no shock wave during the growth phase. As a result, no initial shock phase compressible solution is required. An incompressible BEM code can then be used to simulate most of the bubble period until the end of the bubble collapse where, due to high liquid speeds or to the bubble re-entrant jet impacting on the liquid or on the structure, compressible flow effects prevail again.

Although modifications to the BEM method have been proposed in the literature (Wang & Blake 2010, 2011; Wang 2013), these were based on the assumption of

https://doi.org/10.1017/jfm.2014.394 Published online by Cambridge University Press

weak compressibility, which solves a potential flow around the bubble modified by acoustic energy losses at infinity. This BEM solution remains intrinsically based on values of the velocity potential and its derivatives on the boundaries. As a result, this method cannot capture and resolve any near-field shock waves, supersonic flow, or pressure discontinuities which are essential to include in order to obtain resolved pressure loadings needed to predict material damage. Therefore, in the current study, the solution of the incompressible BEM code is passed to a fully compressible code capable of shock capturing to simulate re-entrant jet impact and bubble ring collapse.

2.1. *Incompressible flow solver*

The potential flow solver we have developed and used in this study is based on a BEM (Chahine & Perdue 1990; Chahine *et al.* 1996; Chahine & Kalumuck 1998*a*). The code solves the Laplace equation, $\nabla^2\phi = 0$, for the velocity potential, ϕ, with the velocity vector defined as $\boldsymbol{u} = \nabla\phi$. A boundary integral method is used to solve the Laplace equation based on Green's theorem:

$$\int_{\Omega} (\phi\nabla^2 G - G\nabla^2\phi)\,\mathrm{d}\Omega = \int_{S} \boldsymbol{n}\cdot[\phi\nabla G - G\nabla\phi]\mathrm{d}S. \tag{2.1}$$

In this expression Ω is the domain of integration having elementary volume $\mathrm{d}\Omega$. The boundary surface of Ω is S, which includes the surfaces of the bubble and the nearby boundaries with elementary surface element $\mathrm{d}S$; $\boldsymbol{n}$ is the local normal unit vector; $G = -1/|\boldsymbol{x}-\boldsymbol{y}|$ is Green's function, where $\boldsymbol{x}$ corresponds to a fixed point in Ω and $\boldsymbol{y}$ is a point on the boundary surface S. Equation (2.1) reduces to Green's formula with $a\pi$ being the solid angle under which x sees the domain, Ω:

$$a\pi\phi(\boldsymbol{x}) = \int_{S}\left[\phi(\boldsymbol{y})\frac{\partial G}{\partial n}(\boldsymbol{x},\boldsymbol{y}) - G(\boldsymbol{x},\boldsymbol{y})\frac{\partial\phi}{\partial n}(\boldsymbol{y})\right]\mathrm{d}S. \tag{2.2}$$

To solve (2.2) numerically, the BEM, which discretizes the surface of all objects in the computational domain into panel elements, is applied.

Equation (2.2) provides a relationship between ϕ and $\partial\phi/\partial n$ at the boundary surface S. Thus, if either of these two variables (e.g. ϕ) is known everywhere on the surface, the other variable (e.g. $\partial\phi/\partial n$) can be obtained.

To advance the solution in time, the coordinates of the bubble and any free-surface nodes, $\boldsymbol{x}$, are advanced according to $\mathrm{d}\boldsymbol{x}/\mathrm{d}t = \nabla\phi$. ϕ on the bubble and free-surface nodes is obtained through the time integration of the material derivative of ϕ, i.e. $\mathrm{d}\phi/\mathrm{d}t$, which can be written as

$$\frac{\mathrm{d}\phi}{\mathrm{d}t} = \frac{\partial\phi}{\partial t} + \nabla\phi\cdot\nabla\phi, \tag{2.3}$$

where $\partial\phi/\partial t$ can be determined from the Bernoulli equation:

$$\rho\left(\frac{\partial\phi}{\partial t} + \frac{1}{2}\nabla\phi\cdot\nabla\phi + gz\right) + p_l = p_\infty. \tag{2.4}$$

Here, p_∞ is the hydrostatic pressure at infinity at $z = 0$ where z is the vertical coordinate, and p_l is the liquid pressure at the bubble surface, which balances the internal pressure and surface tension,

$$p_l = p_v + p_g - \sigma\mathscr{C}, \tag{2.5}$$

https://doi.org/10.1017/jfm.2014.394 Published online by Cambridge University Press

where p_v is the vapour pressure, σ is the surface tension and $\mathscr{C}$ is the local bubble wall curvature. Finally, p_g is the gas pressure inside the bubble and is assumed to follow a polytropic law with a compression constant, k, which relates the gas pressure to the gas volume, $\mathscr{V}$, and reference value, p_{g0}, and $\mathscr{V}_0$.

$$p_g = p_{g0}\left(\frac{\mathscr{V}}{\mathscr{V}_0}\right)^k. \tag{2.6}$$

2.2. *Compressible flow solver*

The multi-material compressible Euler equation solver used here is based on a finite difference method (Wardlaw *et al.* 2003). The code solves continuity and momentum equations for a compressible inviscid liquid in Cartesian coordinates. These can be written in the following format:

$$\frac{\partial \boldsymbol{Q}}{\partial t} + \frac{\partial \boldsymbol{E}}{\partial x} + \frac{\partial \boldsymbol{F}}{\partial y} + \frac{\partial \boldsymbol{G}}{\partial z} = \boldsymbol{S}, \tag{2.7}$$

$$\left.\begin{aligned} \boldsymbol{Q} &= \begin{bmatrix} \rho \\ \rho u \\ \rho v \\ \rho w \\ \rho e_t \end{bmatrix}, \quad \boldsymbol{E} = \begin{bmatrix} \rho u \\ \rho u^2 + p \\ \rho uv \\ \rho uw \\ (\rho e_t + p)u \end{bmatrix}, \quad \boldsymbol{F} = \begin{bmatrix} \rho v \\ \rho vu \\ \rho v^2 + p \\ \rho vw \\ (\rho e_t + p)v \end{bmatrix}, \\ \boldsymbol{G} &= \begin{bmatrix} \rho w \\ \rho wu \\ \rho wv \\ \rho w^2 + p \\ (\rho e_t + p)w \end{bmatrix}, \quad \boldsymbol{S} = \begin{bmatrix} 0 \\ 0 \\ 0 \\ \rho g \\ \rho gw \end{bmatrix}, \end{aligned}\right\} \tag{2.8}$$

where ρ is the fluid density, p is the pressure, u, v and w are the velocity components in the x, y, z directions respectively (z is vertical), g is the acceleration due to gravity, and $e_t = e + 0.5(u^2 + v^2 + w^2)$ is the total energy with e being the internal energy. The system is closed by using an equation of state for each material, which provides the pressure as a function of the material specific internal energy and the density. Here, a γ-law (with $\gamma = 1.4$) is used for the gas–vapour mixture (Anderson 1990):

$$p = (\gamma - 1)\rho e, \tag{2.9}$$

and the Tillotson equation is used for water (Zel'Dovich & Raizer 2002):

$$p = p_0 + \omega\rho(e - e_0) + A\mu + B\mu^2 + C\mu^3, \quad \mu = \frac{\rho}{\rho_0} - 1. \tag{2.10}$$

ω, A, B, C are constants and p_0, e_0 and ρ_0 are the reference pressure, specific internal energy, and density respectively: $\omega = 0.28$, $A = 2.20 \times 10^9$ Pa, $B = 9.54 \times 10^9$ Pa, $C = 1.48 \times 10^{10}$ Pa, $e_0 = 3.54 \times 10^5$ m^2 s^{-2}, $p_0 = 1.0 \times 10^5$ Pa, $\rho_0 = 1000$ kg m^{-3}.

The compressible flow solver uses a high-order Godunov scheme. It employs the Riemann problem to construct a local flow solution between adjacent cells. The numerical method is based on a higher-order MUSCL scheme and tracks each material. To improve efficiency, an approximate Riemann problem solution replaces the full problem. The MUSCL scheme is augmented with a mixed cell approach

https://doi.org/10.1017/jfm.2014.394 Published online by Cambridge University Press

(Colella 1985) to handle shock wave interactions with fluid or material interfaces. This approach uses a Lagrangian treatment for the cells including an interface and an Eulerian treatment for cells away from interfaces. A re-map procedure is employed to map the Lagrangian solution back to the Eulerian grid. The code has been extensively validated against experiments (Wardlaw *et al.* 2003; Kapahi, Hsiao & Chahine 2014).

2.3. *Compressible–incompressible link procedure*

Both incompressible and compressible flow solvers are able to model the full bubble dynamics on their own. However, each method has its shortcomings when it comes to specific parts of the bubble history. The BEM-based incompressible flow solver is efficient, reduces the dimension of the problem by one (line integrals for an axisymmetric problem, and surface integrals for a three-dimensional problem) and thus allows very fine gridding and increased accuracy with reasonable computations times. It has been shown to provide re-entrant jet parameters and speed accurately (Chahine & Perdue 1990; Zhang *et al.* 1993; Chahine *et al.* 2006; Jayaprakash *et al.* 2012). However, it has difficulty pursuing the computations beyond surface impacts (liquid–liquid and liquid–solid).

On the other hand, the compressible flow solver is most adequate to model shock wave emission and propagation, liquid–liquid, and liquid–solid impacts. The method requires, however, very fine grids and very small time steps to resolve shock wavefronts. This makes it appropriate to model time portions of the bubble dynamics. Concerning the bubble–liquid interface and the re-entrant jet dynamics, the procedure is diffusive since the interface is not directly modelled, and re-entrant jet characteristics are usually less accurate than obtained with the BEM approach.

Hence a general novel approach would combine the advantages of both methods and would consist in executing the following steps:

(i) Set up the initial flow field using the Eulerian compressible flow solver and run the simulation until the initial shock fronts have passed by and the remnant flow field can be assumed to be incompressible with bubble dynamics independent of initial treatments.

(ii) Transfer at that instant to the Lagrangian BEM potential flow solver 3DynaFS all the flow field variables needed by the solver: geometry, bubble pressure, boundary velocities to specify the moving boundary's normal velocities, $\partial\phi/\partial n$.

(iii) Solve for bubble growth and collapse using fine BEM grids to obtain a good description of the re-entrant jet until the point where the jet is very close to the opposite side of the bubble.

(iv) Transfer the solution back to the compressible flow solver with the required flow variables. To do so, compute using the Green equation all flow field quantities on the Eulerian grid.

(v) Continue solution progress with the compressible code to obtain pressures due to jet impact and remnant bubble ring collapse.

2.4. *Structure dynamics solver*

To model the dynamics of the material, the finite element model Dyna3D is used. Dyna3D is a nonlinear explicit structure dynamics code developed by the Laurence Livermore National Laboratory. Here it computes the material deformation when the loading is provided by the fluid solution. Dyna3D uses a lumped mass formulation for efficiency. This produces a diagonal mass matrix $\boldsymbol{M}$, to express the momentum

https://doi.org/10.1017/jfm.2014.394 Published online by Cambridge University Press

Metallic material	Yield stress (MPa)	Young's modulus (GPa)	Tangent modulus (MPa)	Elongation at break	Density (g cm^{-3})
Al7075	503	71.7	670	0.11	2.81
A2205	515	190	705	0.35	7.88

TABLE 1. Material properties of the metal alloys investigated in this study.

Compliant material	Shear modulus (MPa)	Density (g cm^{-3})
Rubber 1 (neoprene)	99.7	1.18
Rubber 2 (polyurethane)	34.17	1.20

TABLE 2. Material properties of the two rubbers investigated in this study.

equation as:

$$\boldsymbol{M}\frac{\mathrm{d}^2\boldsymbol{x}}{\mathrm{d}t^2} = \boldsymbol{F}_{ext} - \boldsymbol{F}_{int}, \tag{2.11}$$

where $\boldsymbol{F}_{ext}$ represents the applied external forces, and $\boldsymbol{F}_{int}$ the internal forces. The acceleration, $\boldsymbol{a} = \mathrm{d}^2\boldsymbol{x}/\mathrm{d}^2t$ for each element, is obtained through an explicit temporal central difference method. Additional details on the general formulation can be found in Whirley & Engelmann (1993).

2.5. *Material models*

In the present study, two metal alloys (aluminium 7075 and stainless steel A2205), two rubbers (a neoprene synthetic rubber and a polyurethane), and a Versalink based polyurea are considered. The metals are modelled using elastic–plastic models with linear slopes (moduli), one for the initial elastic regime and the second, a tangent modulus, for the plastic regime. The material parameters of the metal alloys used in this study are shown in table 1.

For the rubbers, a Blatz–Ko hyper-elastic model is used. This model is appropriate for materials undergoing moderately large strains and is based on the implementation in Key (1974). The material motion satisfies the formal equation

$$\rho_s\frac{\mathrm{d}^2\boldsymbol{x}}{\mathrm{d}t^2} = \nabla\cdot\boldsymbol{\sigma}, \tag{2.12}$$

where ρ_s is the material density, $\boldsymbol{x}$ is the position vector of the material and $\boldsymbol{\sigma}$ is the Cauchy stress tensor. If we denote $\boldsymbol{F}$ the deformation gradient tensor, then the Cauchy stress tensor is computed by

$$\boldsymbol{\sigma} = \frac{1}{J}\boldsymbol{F}\boldsymbol{S}\boldsymbol{F}^{\mathrm{T}}, \tag{2.13}$$

where J is the determinant of $\boldsymbol{F}$ and $\boldsymbol{S}$ is the second Piola–Kirchoff stress tensor and is computed by

$$S_{ij} = G(C_{ij}/V - V^{-1/(1-2\nu)}\delta_{ij}). \tag{2.14}$$

G is the shear modules, V is the volume relative to the original which is related to excess compression and density, C_{ij} is the right Cauchy–Green strain tensor, and ν is Poisson's ratio and is set to 0.463. Table 2 shows the material parameters of the

https://doi.org/10.1017/jfm.2014.394 Published online by Cambridge University Press

two rubbers of different strengths. Rubber 1 is approximately three times stiffer than rubber 2.

The Versalink-based polyurea was modelled as a viscoelastic material with the following time-dependent values for the shear modulus, G:

$$G(t) = G_\infty + (G_o - G_\infty)\mathrm{e}^{-\beta t}, \tag{2.15}$$

with

$$G_\infty = 41.3\ \text{MPa}, \quad G_o = 79.1\ \text{MPa}, \quad K = 4.948\ \text{GPa}, \quad \beta = 15\,600\ \text{s}^{-1}. \tag{2.16a–d}$$

While the time dependence of G is considered in this model, the bulk modulus, K, was assumed to be constant. The material parameters in (2.16) are derived from simplification of fourth-order Prony series in Amirkhizi *et al.* (2006) taking the second term as the major contributor.

2.6. *Fluid–structure interaction coupling*

Fluid–structure interaction effects are captured in the simulations by coupling the fluid codes and DYNA3D through a coupler interface. The coupling is achieved through the following steps:

(i) The fluid code solves the flow field and deduces the pressures at the structure surface using the positions and normal velocities of the wetted body nodes.
(ii) In response, the structure code computes material deformations and velocities in response to this loading.
(iii) The new coordinates and velocities of the structure surface nodes become the new boundary conditions for the fluid code at the next time step.

Additional details on the procedure can be found in Chahine & Kalumuck (1998*a*,*b*) and Wardlaw & Luton (2000). This FSI coupling procedure has only a first-order time accuracy. A predictor–corrector approach is also implemented in the coupling to iterate and improve the solution but was not used here. This is because the numerical error due the time lag is negligible thanks to the very small time steps used. These are controlled by the steep pressure waves, which have a time scale that is two orders of magnitude shorter than the time response of the material. This method has been shown in UNDEX studies to correlate very well with experiments (Harris *et al.* 2009).

3. Problem definition

3.1. *Pressure field driving bubble collapse*

It is known that microbubbles or nuclei are always present in liquids and are entrained in the flow (Brennen 1995). Also nano-cavities at the solid surfaces and solid particles in the fluid serve as nucleation sites for the formation of microbubbles under cavitating conditions. Once excited by local pressures decreasing below a critical value (Chahine & Shen 1986), bubbles grow explosively until their internal pressure drops below the surrounding local pressure. The bubbles can then collapse violently, producing intense pressures, emitting sound, and eroding any solid surfaces in their proximity.

To mimic such a cavitation scenario in this contribution, we consider a nucleus initially at equilibrium with the surrounding liquid and subject it to a time-dependent pressure field, which would correspond to what it would see while moving in the flow close to the material surface. As illustrated in figure 2 the pressure first drops

https://doi.org/10.1017/jfm.2014.394 Published online by Cambridge University Press

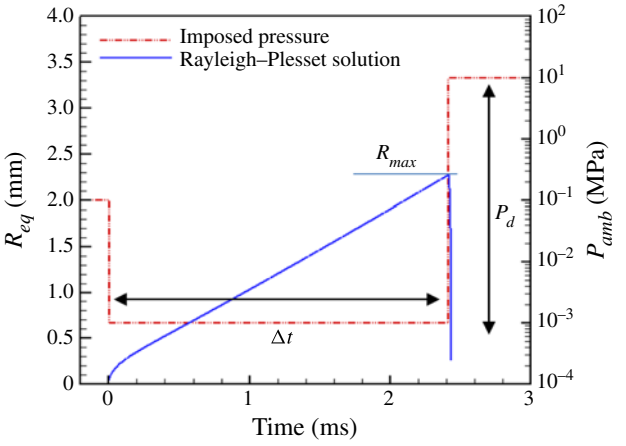


FIGURE 2. (Colour online) Imposed time-dependent pressure field (dot-dashed curve) around an initially spherical bubble of 50 μm radius, and resulting bubble radius versus time (solid curve) as predicted by the solution of the Rayleigh–Plesset equation.

to a value below the bubble critical pressure and then remains at this pressure for a prescribed time, Δt. The pressure then rises to a high value and remains there until the end of the computation.

Figure 2 illustrates this for the case of a bubble of initial radius $R_0 = 50$ μm at equilibrium in the liquid at 1 atm (10^5 Pa). The pressure then suddenly decreases to 10^3 Pa, stays there for $\Delta t = 2.415$ ms, and then rises sharply to $P_d = 10$ MPa, which is commonly encountered in cavitation erosion measurement (Chahine 2014). Figure 2 also shows the response of a hypothetical spherical bubble to this pressure function obtained by integrating the Rayleigh–Plesset equation. It is seen that as soon as the ambient pressure drops to the low 10^3 Pa value, the bubble responds and starts growing. Since the ambient pressure drops below the bubble critical pressure (Chahine 1993, 2014) the bubble cannot reach an equilibrium size and continues to grow during Δt until the sudden pressure rise to 10 MPa occurs. A maximum bubble size, R_{max}, is reached a little time after the overpressure is imposed due to liquid inertia. This is followed by a strong collapse of the bubble.

3.2. *Numerical discretization*

To simulate the bubble dynamics with the incompressible BEM solver, a total of 400 nodes and 800 panels were used to discretize the bubble surface. This corresponds to a grid density which provides grid-independent solution (Chahine *et al.* 1996). The FSI simulations were conducted during the bubble collapse phase when the stresses were of consequence to the material response or deformation. An axisymmetric domain with a total of 220 × 1470 grid points was used with a stretched grid in a 1 m × 1 m domain concentrating the grids in the immediate region surrounding the bubble. The grid was distributed such that there was a uniform fine mesh with a size of 10 μm covering the area of interest where the interaction between bubble and plate is important as shown in figure 3. The axisymmetric computational domain was bounded at selected distances in the far field (radial direction and away from the wall) and at the plate material wall for FSI simulations.

A reflection boundary condition was imposed on the axis of symmetry, i.e. all physical variables such as density, pressure, velocities and energy are reflected from

https://doi.org/10.1017/jfm.2014.394 Published online by Cambridge University Press

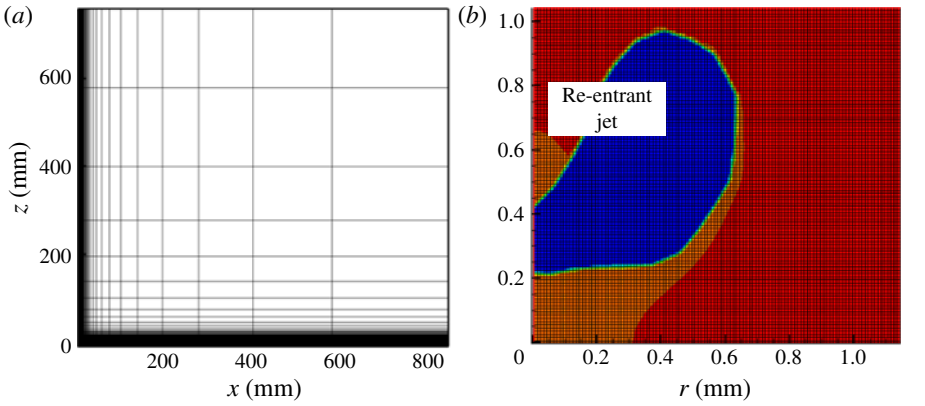


FIGURE 3. (Colour online) Axisymmetric computational domain used for the computation of the bubble dynamics by the compressible flow solver: (*a*) full domain, (*b*) zoomed area at the bubble location. The dark region is the inside of the bubble after it formed a re-entrant jet on the axis of symmetry.

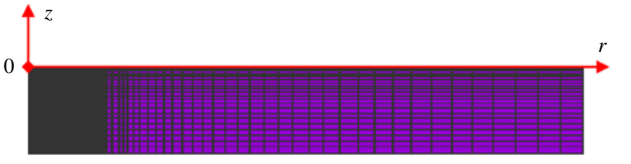


FIGURE 4. (Colour online) Finite element axisymmetric grid used in DYNA3D to study the material response to loads due to collapsing cavitation bubbles.

the axis, while transmission non-reflective boundary conditions, i.e. the flow variables are extrapolated along the characteristic wave direction, were imposed at the far-field boundaries.

For the structure computations, axisymmetry was used and a circular plate with a radius of 1 m and a thickness of 0.01 m was discretized using rectangular brick elements. As shown in figure 4(*a*) stretched grid with 220 elements in the radial direction, r, and 446 elements in the axial direction, z, were used to discretize the plate. The elements were distributed such that a uniform fine mesh size of 10 μm existed near the centre of the plate where the high-pressure loading occurs. Other mesh sizes were also tested to establish convergence and grid independence of the solution. The motion of the nodes at the plate bottom was restricted in all directions. The nodes along the vertical axis were only allowed to move in the vertical direction.

4. Material pitting simulations

4.1. *Generation of loads*

Let us consider, as a base case, an initially spherical bubble of radius 50 μm, located at a distance of $X = 1.5$ mm from a flat material surface and subjected to an imposed pressure field as represented in figure 2. The time dependence of this pressure can be

https://doi.org/10.1017/jfm.2014.394 Published online by Cambridge University Press

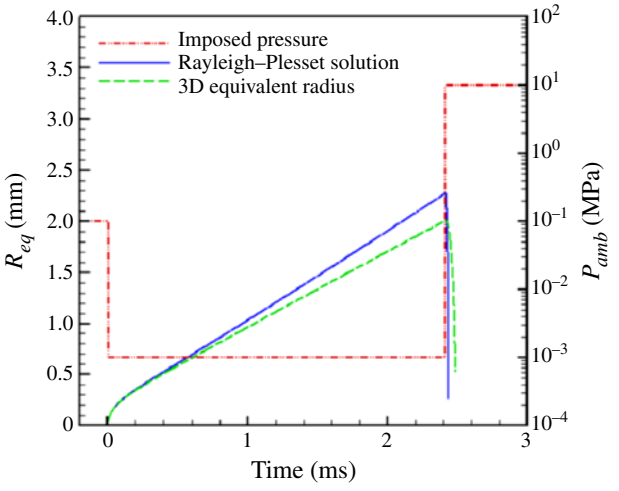


FIGURE 5. (Colour online) Comparison of the equivalent radius versus time of the deforming bubble with the Rayleigh–Plesset solution. Initially spherical bubble of 50 μm radius located at a distance of $X = 1.5$ mm above a flat material surface and subjected to the pressure field as described by (4.1).

written as follows:

$$p(t) = \begin{cases} 10^5 \text{ Pa}; & t < 0, \\ 10^3 \text{ Pa}; & 0 \leqslant t \leqslant 2.415 \text{ ms}, \\ 10^6 \text{ Pa}; & t > 2.415 \text{ ms}. \end{cases} \tag{4.1}$$

The bubble dynamics near the wall up to the point of re-entrant jet impact can be simulated using the three-dimensional BEM solver. Figure 5 compares the bubble radius versus time between the Rayleigh–Plesset solution and the three-dimensional solution. The three-dimensional dynamics results in a reduction of the bubble maximum volume relative to the free-field Rayleigh–Plesset solution due to material wall confinement effects.

Figure 6 shows the variations of the bubble outer contour versus time. As the bubble grows between $t = 0$ and $t \sim 2.4$ ms, it behaves almost spherically on its portion away from the wall, while the side close to the material flattens and expands in the direction parallel to the wall actually never touching the wall as a layer of liquid remains between the bubble and the wall. Such a behaviour has been confirmed experimentally by Chahine *et al.* (1996). Note that at maximum bubble volume, the non-dimensional standoff, $\bar{X} = X/R_{max}$, is 0.75 (less than one) where R_{max} is the maximum equivalent bubble radius deduced from its volume.

The bubble will continue expanding at the starting of reverse pressure due to the inertia of the outward flow of the liquid. Due to the asymmetry of the flow, the pressures at the bubble interface on the side away from the wall are much higher than those near the material; thus the collapse proceeds with the far side moving towards the material wall. The resulting acceleration of the liquid flow perpendicular to the bubble free surface develops a Taylor instability at the axis of symmetry, which results in a re-entrant jet that penetrates the bubble and moves much faster than the rest of the bubble surface to impact on the opposite side of the bubble and the material boundary.

https://doi.org/10.1017/jfm.2014.394 Published online by Cambridge University Press

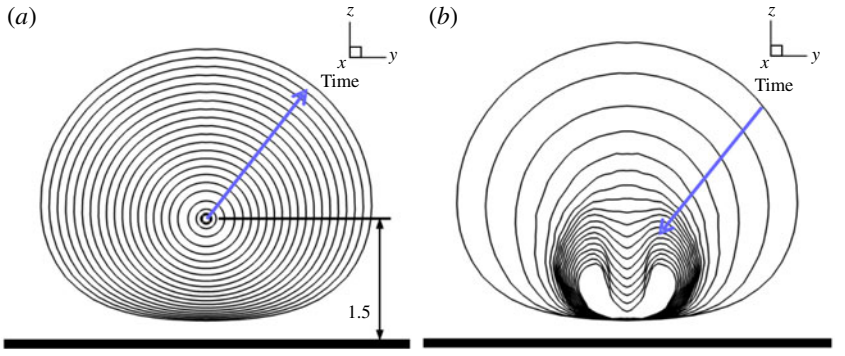


FIGURE 6. (Colour online) Bubble shape outlines at different times showing (*a*) bubble growth ($0 < t < 2.415$ ms) and (*b*) collapse ($2.415 < t < 2.435$ ms). Results obtained from the three-dimensional BEM simulations for $R_0 = 50$ μm, $P_d = 10$ MPa, $\bar{X} = 0.75$, and $p(t)$ described by (4.1).

In the present approach, the simulation of the bubble dynamics is switched from the BEM to the compressible solver just before the jet touches the opposite side of the bubble. Ideally, the time of the switch, the 'link' time, should be the time at which the bubble becomes multi-connected. However, to avoid increased errors/fluctuations in the BEM solution when the distance between a jet panel and the opposite bubble side panels continues to decrease as the jet advances, the link time was selected to be when the distance between the jet front and the opposite bubble surface becomes less than or equal to 1.5 times the local panel size. This results in an underestimate of t_{link} by less than 1 %. Figure 7(*a*) shows the pressure contours and velocity vectors at the selected time, t_{link}, when the compressible flow solver and the FSI start their computations. Figure 7(*b*) shows the corresponding velocity vectors and velocity magnitude contour levels. Note that, for this bubble collapse condition, prior to jet impact on the opposite side of the bubble, the liquid velocity near the tip of the jet exceeds 1400 m s^{-1}. The maximum liquid velocity of the jet exceeds the sound speed after the 'link' time when the computation was continued with the compressible code. The peak value reaches approximately 1600 m s^{-1} at the time when the jet touches down on the opposite side of the bubble. The variations of the jet speed with the imposed collapse pressure are discussed further below in the parametric study section.

Figure 8 shows the bubble shapes and corresponding pressure contours computed at six time instances after $t_{link} = 2.435$ ms. It is seen that at $t - t_{link} = 0.05$ μs the jet has completely penetrated the bubble and touched the opposite side. The liquid–liquid impact event generates a localized high-pressure region which then expands quasi-spherically to reach the material liquid interface at $t - t_{link} = 0.2$ μs. The volume of the bubble ring remaining after the jet touchdown shrinks and reaches a minimum at $t - t_{link} = 0.7$ μs. The collapse of the bubble ring generates another high-pressure wave, which then propagates toward the axis of the cylindrical domain and reaches the wall at $t - t_{link} = 0.9$ μs.

To display better the pressure field dynamics during the bubble collapse impulsive loads period, a zoom of the pressure contours in the region between the re-entrant jet impact on the opposite side of the bubble and the rigid wall is shown in figure 9. Eight time steps are selected between the jet impact and the shock wave reflection from the wall. The re-entrant jet impact in figure 9(*a*) forms a strong ellipsoidal

https://doi.org/10.1017/jfm.2014.394 Published online by Cambridge University Press

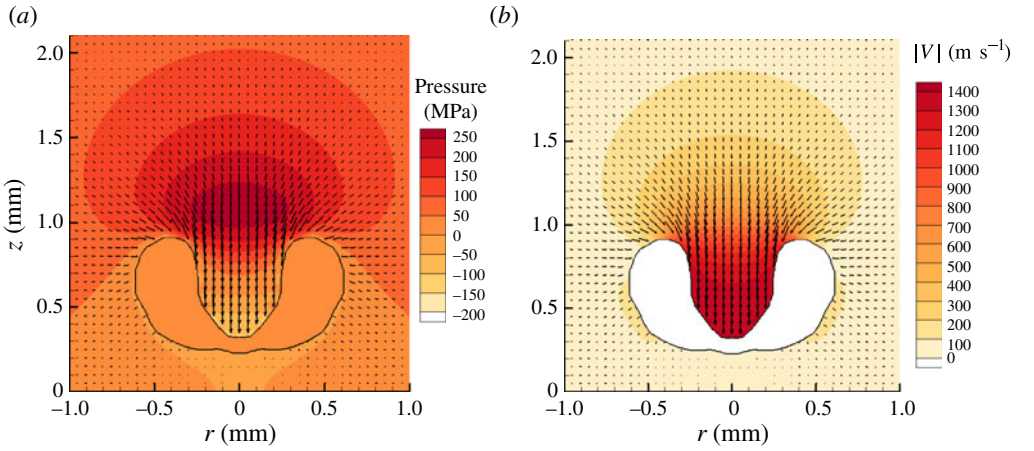


FIGURE 7. (Colour online) (*a*) Pressure contour levels with velocity vectors and (*b*) velocity vectors and magnitude contour levels at $t = 2.435$ ms, the time at which the incompressible–compressible link procedure is applied. These serve as initial conditions for the compressible flow and FSI solvers for $R_0 = 50$ μm, $P_d = 10$ MPa, $\bar{X} = 0.75$ and $p(t)$ described by (4.1).

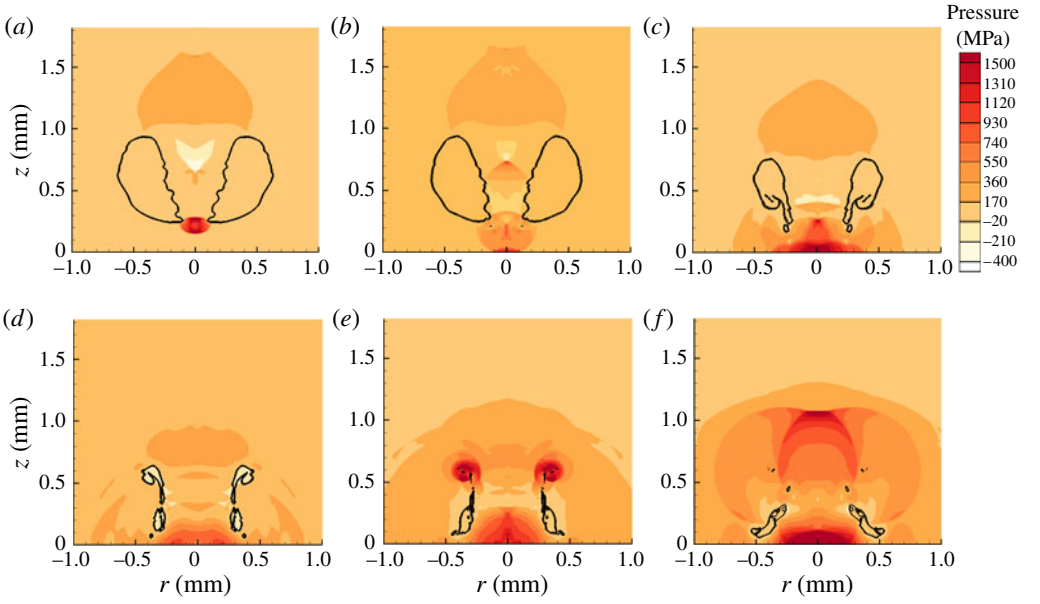


FIGURE 8. (Colour online) Pressure contours at different instances during the bubble collapse near the wall. High pressures are generated by the re-entrant jet impact and by the following bubble ring collapse. The bubble initial radius is $R_0 = 50$ μm, the equivalent radius at maximum is $R_{max} = 2$ mm, the initial standoff is $\bar{X} = 0.75$, and the collapse driving pressure is $P_d = 10$ MPa. (*a*) $t - t_{link} = 0.05$ μs, (*b*) $t - t_{link} = 0.2$ μs, (*c*) $t - t_{link} = 0.4$ μs, (*d*) $t - t_{link} = 0.6$ μs, (*e*) $t - t_{link} = 0.7$ μs, (*f*) $t - t_{link} = 0.9$ μs.

shock wave, which later propagates outwards in all directions losing intensity from reflections into the bubble free surface but remaining strong in the axial region of the bubble (figure 9*b*,*c*). The shock front advances towards the solid wall at the

https://doi.org/10.1017/jfm.2014.394 Published online by Cambridge University Press

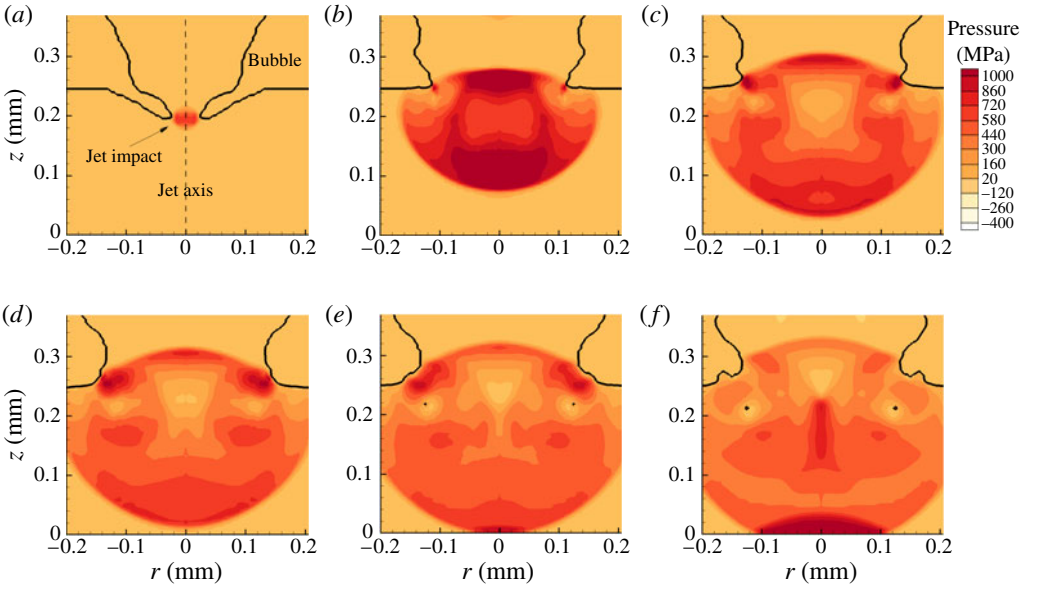


FIGURE 9. (Colour online) Zoom of the region between the re-entrant jet impact on the opposite side of the bubble (shown full size in *a*) and the rigid wall at $z = 0$. Pressure contours at six different times showing the resulting shock wave reaching the wall (between *d* and *e*) and reflecting from it (*e* and *f*). $\bar{X} = 0.75$, $R_0 = 50$ μm, $R_{max} = 2$ mm and $P_d = 10$ MPa. (*a*) $t - t_{link} = 0.04$ μs, (*b*) $t - t_{link} = 0.151$ μs, (*c*) $t - t_{link} = 0.182$ μs, (*d*) $t - t_{link} = 0.189$ μs, (*e*) $t - t_{link} = 0.196$ μs, (*f*) $t - t_{link} = 0.206$ μs.

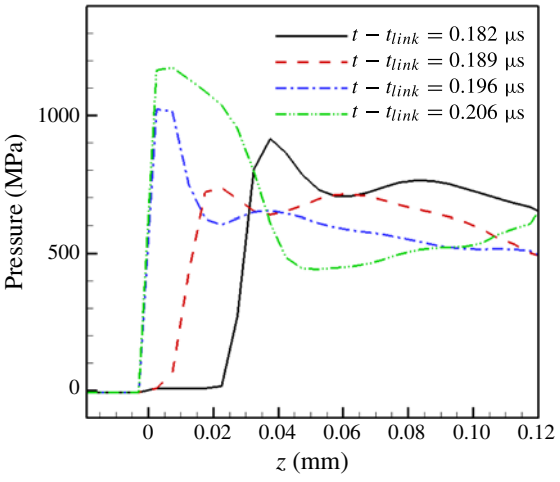


FIGURE 10. (Colour online) Pressure distribution along the axis of symmetry at four times before and after the shock wave from the jet–bubble wall impact reaches the rigid wall. These times correspond to figure 9(*c–f*). $\bar{X} = 0.75$ for $R_0 = 50$ μm, $R_{max} = 2$ mm and $P_d = 10$ MPa.

fluid sound speed and impacts between figures 9(*d*) and 9(*e*). It then reflects as a reinforced reflection wave between 9(*e*) and 9(*f*).

The corresponding pressure distribution along the axis of symmetry at the last four time steps is shown in figure 10. It can be seen that the incoming pressure of

https://doi.org/10.1017/jfm.2014.394 Published online by Cambridge University Press

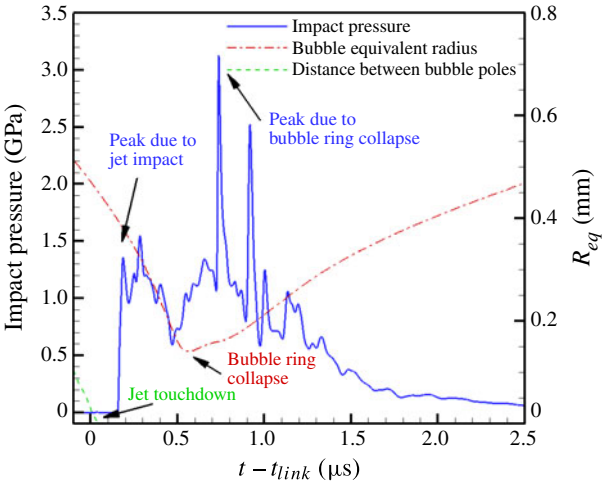


FIGURE 11. (Colour online) Zoom at bubble collapse of the equivalent bubble radius evolution versus time, along with the pressure recorded at the axis on the rigid wall located at a standoff of $\bar{X} = 0.75$ for $R_0 = 50$ μm, $R_{max} = 2$ mm and $P_d = 10$ MPa.

maximum amplitude 700 MPa (dashed curve) is almost doubled following reflection in the rigid wall to approximately 1.3 GPa (dash-dot-dot curve). The magnitude of this high-pressure loading level has been pointed out or deduced from both numerical studies and from experimental measurements (Jones & Edwards 1960; Philipp & Lauterborn 1998; Chahine 2014).

Figure 11 shows the time history of the bubble equivalent radius and the pressure at the axis of symmetry on the wall surface ($z = 0$). One can observe the generation by the bubble collapse of two distinct pressure peaks, one resulting from the re-entrant jet impact at the wall and the other occurring just after the remainder ring bubble reaches its minimum size. In addition to these two peaks, many other pressure peaks are observed due to pressure or shock waves bouncing back and forth between the target wall, the bubble surface, and any other daughter bubbles in the near-wall flow field. The magnitudes of these pressure peaks depend on the level of deformation of the solid material. Figure 12 shows a comparison of the time histories of the collapse impulsive load between a non-deformable wall and an Al7075 deformable plate at the moment when the initial shock wave reaches the wall. The figure shows that the pressure peak felt by the wall is smaller when the solid boundary deforms and absorbs part of the energy.

To ensure that the spatial and temporal resolutions used in most of the cases shown in this paper are small enough to ensure discretization independence, simulations were conducted for different characteristic grid sizes, Δx, and different time steps. The time step size varies during a simulation and is determined by the CFL number according to:

$$\Delta t = \mathrm{CFL}\ \min\left(\frac{\Delta x}{u \pm c}\right), \tag{4.2}$$

where u and c are local fluid velocity and sound speed. $\mathrm{CFL} = 0.45$ is mostly used in this paper. For the spatial resolution study, Δx ranging from 5 to 40 μm was tested with the CFL number adjusted to maintain the same ideal time step size, i.e. Δt is the same for all the cases if the maximum value of $u \pm c$ is the same.

https://doi.org/10.1017/jfm.2014.394 Published online by Cambridge University Press

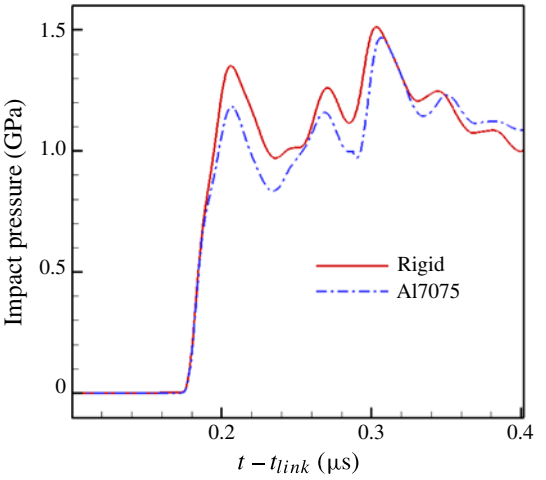


FIGURE 12. (Colour online) Comparison of time history of impact pressure between a rigid wall and an Al7075 deformable plate near the moment of the initial shock wave reaching the wall for $\bar{X} = 0.75$, $R_0 = 50$ μm, $R_{max} = 2$ mm and $P_d = 10$ MPa.

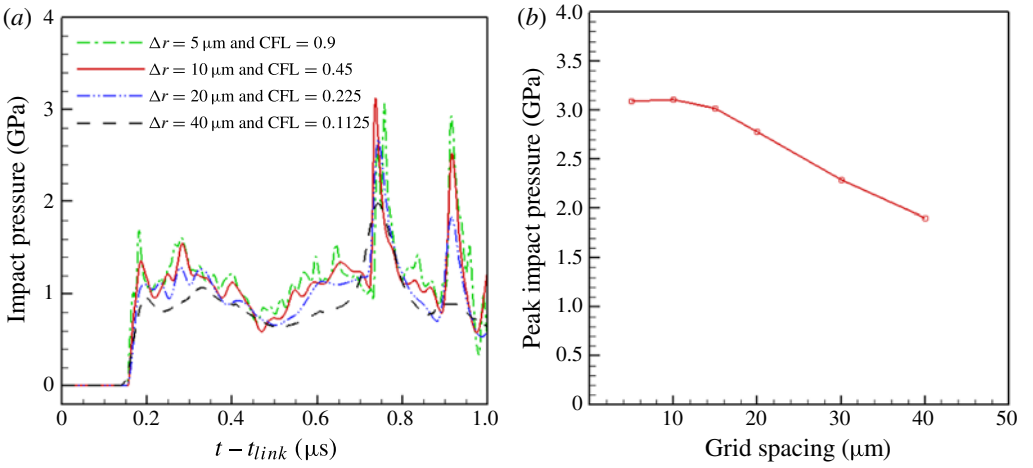


FIGURE 13. (Colour online) (*a*) Comparison of time history of pressure on the wall for four levels of grid sizes and different CFL numbers in an effort to keep the same Δt, and (*b*) the convergence trend of the maximum peak pressure when reducing grid spacing.

The convergence of the spatial resolution is shown in figure 13. It is seen that, except for the very large 40 μm grid, all other resolutions give approximately the same results. The 10 μm case captures very well the magnitude and timing of the main pressure peaks even though further refinement of grid yields additional high-frequency oscillations. Examination of the differences reveals that these oscillations are due to finer interface features, which result in a rougher interface and the detachment of small daughter bubbles from the main bubble, which produce further oscillations of the waves bouncing back and forth between the bubble and solid boundaries. This is illustrated in figure 14, which shows a comparison of the bubble–liquid interface between two values of Δx, 10 and 5 μm. However, these

https://doi.org/10.1017/jfm.2014.394 Published online by Cambridge University Press

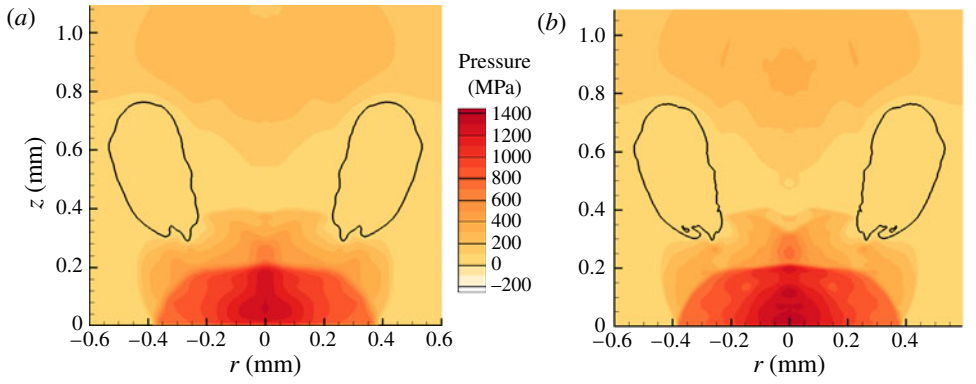


FIGURE 14. (Colour online) Comparison of the bubble–liquid interface (bubble ring cross-section with $r = 0$ being the axis of symmetry) at a selected time between a grid size determined by (*a*) $\Delta x = 10$ μm and (*b*) $\Delta x = 5$ μm. Notice smaller features appearing with the finer grid.

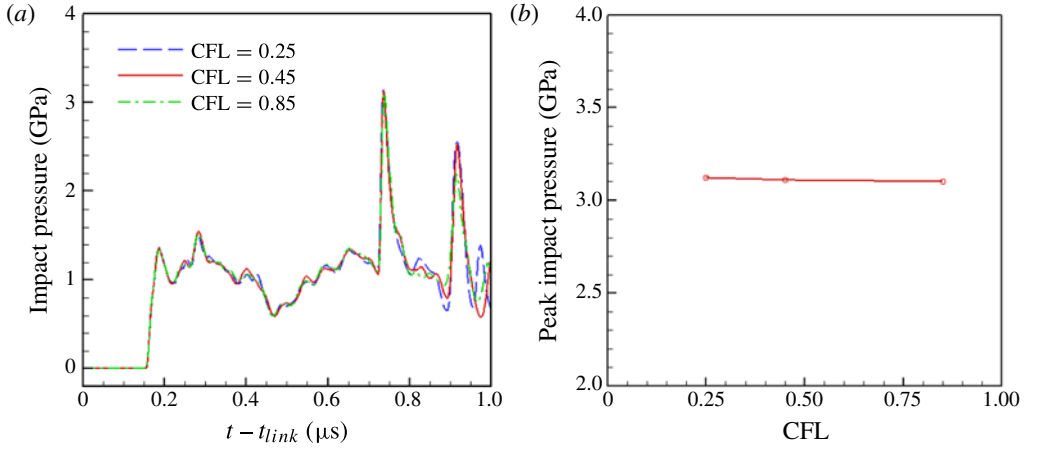


FIGURE 15. (Colour online) (*a*) Comparison of the time history of the pressure on the wall for three CFL numbers for $\Delta x = 10$ μm, and (*b*) convergence trend of the maximum peak pressure with changing CFL number.

high-frequency oscillations do not significantly alter the dynamics of the impact pressure function and the pitting formation and development.

For the temporal resolution study, three different CFL numbers were tested for the same grid size, $\Delta x = 10$ μm. Figure 15 shows the convergence of the peak pressure as obtained for each CFL computations. The figure illustrates that the solution is well resolved and converged with the selected temporal resolution.

4.2. *Material deformation*

As observed experimentally and recovered in the present simulations, the pressures generated by the bubble collapse and rebound are at least two orders of magnitude higher than the pressures generated during the rest of the bubble period. In order to evaluate whether, under the present conditions, ignoring FSIs before bubble collapse

https://doi.org/10.1017/jfm.2014.394 Published online by Cambridge University Press

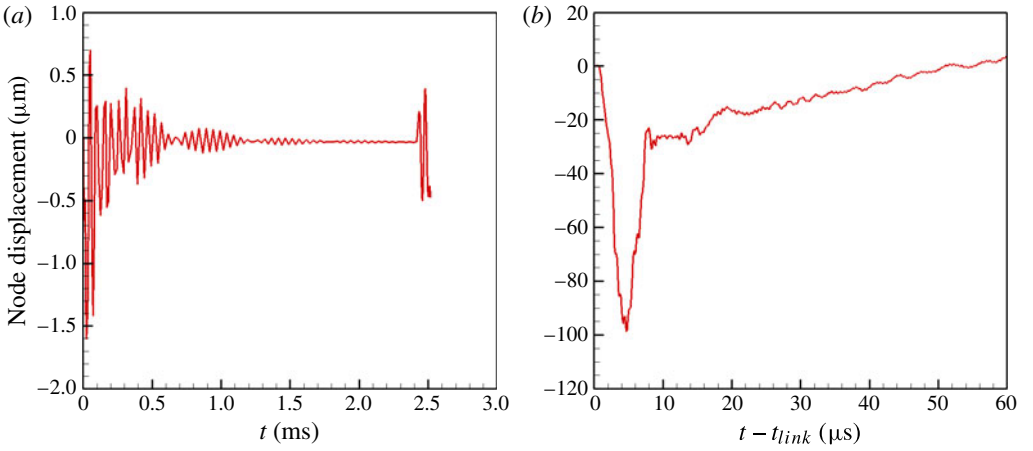


FIGURE 16. (Colour online) Time history of the vertical displacement monitored at the centre location of the rubber plate top surface: (*a*) during the bubble growth phase before the incompressible–compressible link and (*b*) after the link, for $R_0 = 50$ μm, $R_{max} = 2.0$ mm, $P_d = 0.5$ MPa and $\bar{X} = 0.75$.

and re-entrant jet impact have any significant influence on the computations of cavitation pit formation, we analyse a full-period FSI computation for the base-case bubble dynamics conditions near the softest material (rubber 1) in table 2. We concentrate first on the material maximum deformation location. Figure 16 shows the time history of the vertical displacement of the material surface at the centre of the rubber plate. Figure 16(*a*) shows the deformation during the bubble growth and initial collapse phase captured by the coupled BEM/DYNA3D code (the corresponding bubble radius versus time is shown in figure 17). The soft rubber is seen to react to the initial sharp pressure drop (see figure 2) by bulging out and then oscillating up and down at its own resonance frequency, which is much higher than the present bubble excitation frequency. The bubble growth does not add any significant enhancement to the initial pressure perturbation and the rubber material returns practically to its initial stage until the bubble contents start to recompress and the pressures in the liquid start to rise rapidly. This again excites the material into small oscillations. We should note, however, that during this whole period the deformations remain of the order of 1 μm. The computations are pursued beyond $t_{link} \simeq 2.51$ μs using the coupled compressible and solid codes and the resulting material deformation at the plate centre are shown in figure 16(*b*). During this phase the pressures increase significantly (as shown in figure 11) and the material deformation is two orders of magnitude higher than during the bubble growth due to bubble re-entrant jet impact and remaining bubble ring collapse. The maximum deformation generated by the bubble collapse is 100 μm and is shown using different vertical and horizontal scales than in figure 16(*a*). For this 'worst-case' condition amongst the cases considered here, the initial material deformation is only of the order of 1 % of the deformations due to bubble collapse.

Figure 17 illustrates the importance of the inclusion of FSI during the bubble growth phase on the bubble dynamics. The time history of the bubble radius is compared between coupled (FSI) and uncoupled simulations. Here again, the influence of the initial rubber motion on the bubble dynamics is less than 1 %.

https://doi.org/10.1017/jfm.2014.394 Published online by Cambridge University Press

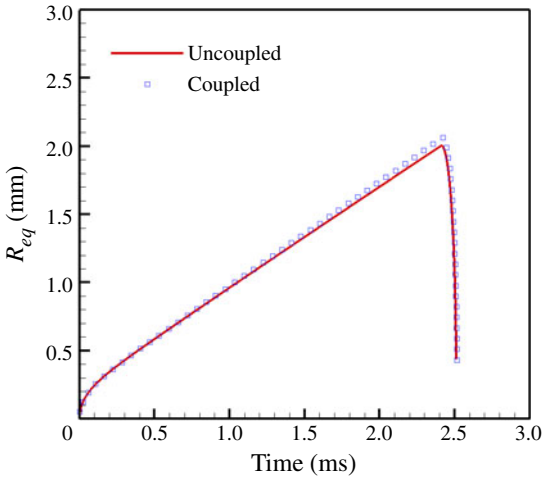


FIGURE 17. (Colour online) Comparison of the bubble equivalent radius between coupled (FSI) and uncoupled (non-FSI) simulations during the bubble dynamics before the incompressible–compressible link for $R_0 = 50$ μm, $R_{max} = 2$ mm, $P_d = 0.5$ MPa and $\bar{X} = 0.75$.

Since material deformation during bubble dynamics up to re-entrant jet impact has very little influence on the re-entrant jet impact and bubble ring collapse phases, FSI simulations in the remainder of the cases presented in this paper are only carried out after the link, i.e. using only the compressible model and solid deformation simulations.

Figure 18 shows a time sequence of the contours of the von Mises equivalent stresses in the material for one of the two metallic alloys considered here, Al7075. It is seen that high stresses appear at the plate centre near the surface when the re-entrant jet impact pressure reaches the wall at $t - t_{link} = 0.2$ μs. The high-stress wave is observed to propagate and move radially away from the impact location. As the first high-stress wave starts to attenuate, another high-stress wave is observed initiating from the top centre of the plate at $t - t_{link} = 0.9$ μs, the time at which the high-pressure wave generated by the collapse of the remaining bubble ring reaches the wall (see figure 8*f*). It is interesting to note that the speed of stress wave propagation in the longitudinal direction (along the axis of symmetry) is approximately 3700 m s^{-1}, i.e. significantly smaller than the expected 6400 m s^{-1} longitudinal wave speed in Al7075. This is due to the plastic deformation of the material, which modifies the material properties and wave behaviour.

All high stresses due to the bubble dynamics eventually attenuate. However, residual stresses remain below the plate surface due to the plastic deformations of the material. In the conditions of figure 18, these have their highest value occurring at a depth of 0.2 mm below the surface as shown in figure 18(*f*). Since the material is modelled as elastic–plastic, permanent deformation should occur wherever the local equivalent stresses exceed the material yield point. With the yield stress of Al7075 being 503 MPa, all regions that have seen the highest stress contour level shown in figure 18 experience permanent deformation due to either re-entrant jet impact or bubble ring collapse.

To quantitatively examine the material response to the pressure loading, the time histories of the liquid pressure and the vertical displacement of the material surface

https://doi.org/10.1017/jfm.2014.394 Published online by Cambridge University Press

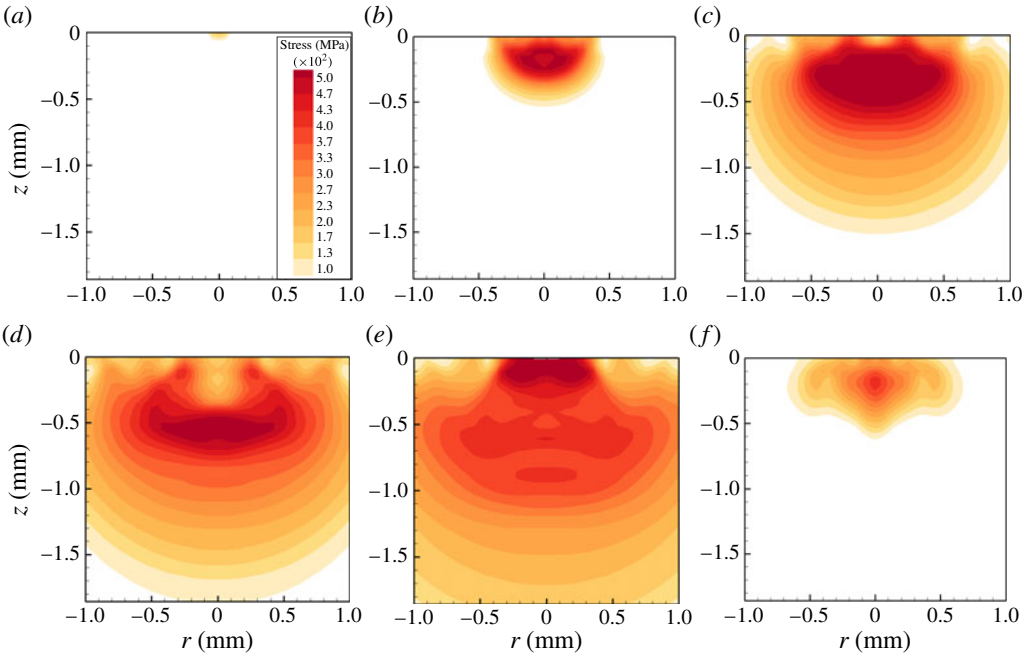


FIGURE 18. (Colour online) Time sequence of the equivalent stress contours in the Al7075 plate for $R_0 = 50$ μm, $R_{max} = 2.0$ mm, $P_d = 10$ MPa and $\bar{X} = 0.75$. (*a*) $t - t_{link} = 0.2$ μs, (*b*) $t - t_{link} = 0.4$ μs, (*c*) $t - t_{link} = 0.6$ μs, (*d*) $t - t_{link} = 0.7$ μs, (*e*) $t - t_{link} = 0.9$ μs, (*f*) $t - t_{link} = 4.0$ μs.

at the centre of the Al7075 plate/liquid interface are shown together in figure 19. The material starts to get compressed as the high-pressure loading due to the re-entrant jet impact reaches it, and the plate surface centre point starts to move in at $t - t_{link} = 0.45$ μs. The maximum deformation occurs when the highest pressure loading peak due to the bubble ring collapse reaches the centre of the plate at time $t - t_{link} = 1.15$ μs. Once the pressure loading due to the full bubble dynamics has virtually vanished at $t - t_{link} = 4$ μs, the surface elevation continues to oscillate due to stress waves propagating back and forth through the metal alloy thickness and lack of damping in the model. Finally, a permanent deformation (pit) remains as a result of the high-pressure loading causing local stresses that exceed the Al7075 elastic limit. As shown in the figure 19, the vertical displacement of the monitored location eventually converges to a non-zero value (∼9 μm).

The radial extent of the permanent deformation is shown in figure 20. The profile of the permanent deformation generated on the plate surface reproduces that of the observed pit shapes (Philipp & Lauterborn 1998; Kim *et al.* 2014). To further study the effect of different parameters on pit formation, we define the pit depth and the pit radius based on the pit profile as follows: the pit depth is the permanent deformation measured at the centre location of the plate/liquid interface and the pit radius is the radial location where the vertical displacement is smaller than 1 μm.

4.3. *Parametric study*

In order to study the influence of various parameters that affect the bubble dynamics and subsequently the coupled material response, a set of parametric simulations are

https://doi.org/10.1017/jfm.2014.394 Published online by Cambridge University Press

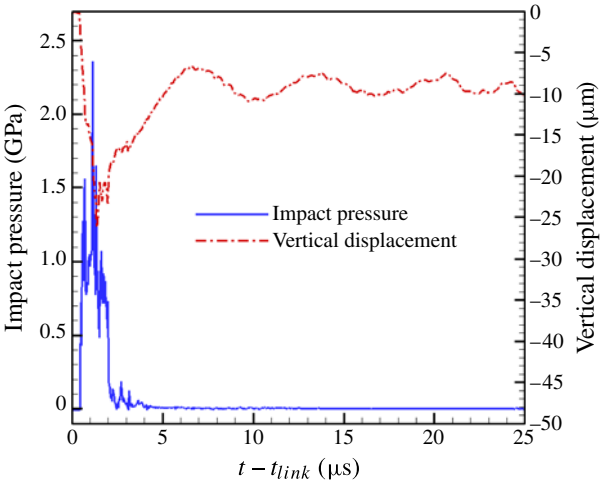


FIGURE 19. (Colour online) Time history of pressure and vertical displacement monitored at the centre location of the Al7075 plate top surface following the collapse of a cavitation bubble near the plate for $R_0 = 50$ μm, $R_{max} = 2.0$ mm, $P_d = 10$ MPa and $\bar{X} = 0.75$.

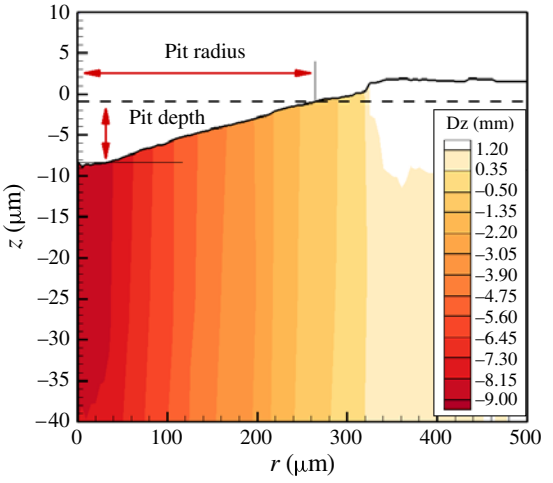


FIGURE 20. (Colour online) Profile of the permanent deformation an Al7075 plate surface following the collapse of a cavitation bubble for $R_0 = 50$ μm, $R_{max} = 2.0$ mm, $P_d = 10$ MPa and $\bar{X} = 0.75$.

presented below. The investigated parameters include: (*a*) the collapse driving pressure, P_d, (*b*) the bubble equivalent radius at its maximum volume, R_{max}, and (*c*) the bubble–wall non-dimensional standoff distance, $\bar{X} = X/R_{max}$. For each parametric study, the same conditions as those for the base representative case shown above are conserved except for the variations of the parameter under consideration.

4.3.1. *Effect of collapse driving pressure*

The pressure driving the bubble collapse (liquid local pressure field value responsible for bubble collapse) is a very important parameter affecting the bubble dynamics, as it is known that the velocity of the collapsing bubble walls varies as the

https://doi.org/10.1017/jfm.2014.394 Published online by Cambridge University Press

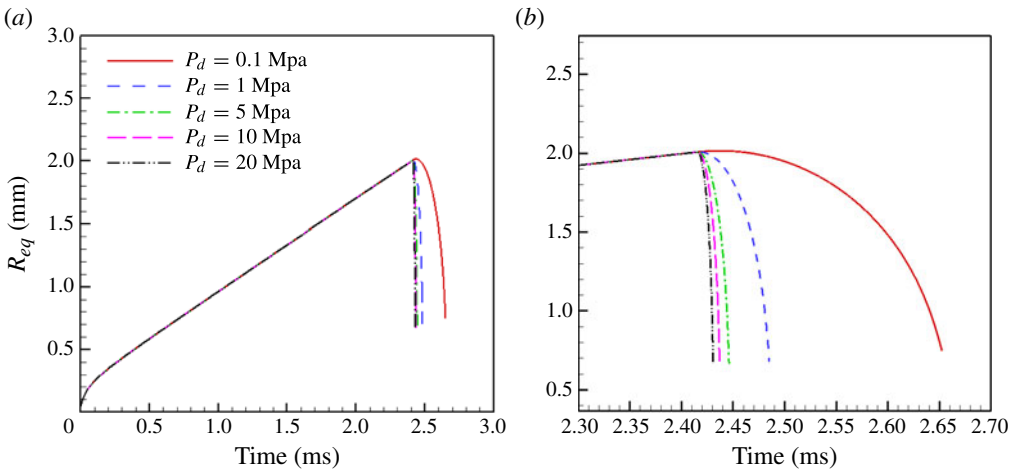


FIGURE 21. (Colour online) Comparison of the bubble equivalent radius for different collapse driving pressures, P_d: (*a*) full history, (*b*) zoom of the collapse period for $R_0 = 50$ μm, $R_{max} = 2$ mm and $\bar{X} = 0.75$.

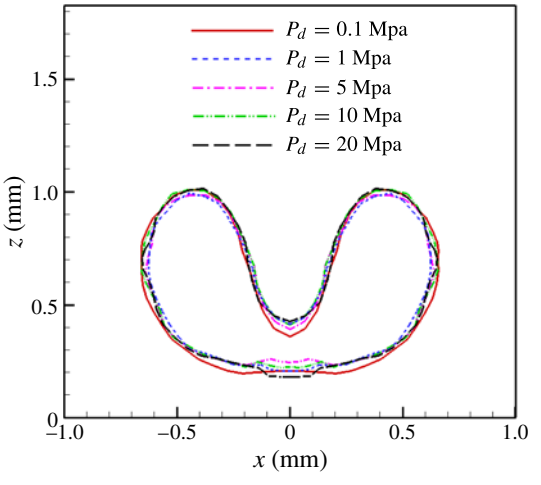


FIGURE 22. (Colour online) Bubble contours at the time of the incompressible/compress ible link for different collapse driving pressures. $R_0 = 50$ μm, $R_{max} = 2$ mm and $\bar{X} = 0.75$.

square root of that pressure (Chahine *et al.* 2006; Jayaprakash *et al.* 2012; Chahine 2014). In this section we vary the magnitude of the collapse driving pressure, P_d, to study its effect on the resulting material pitting. Figure 21 shows the time history of the equivalent radius of the bubble for a set of values of pressure P_d between 0.1 and 20 MPa. In all cases shown, the bubble starts with a $R_0 = 50$ μm nucleus, then grows to a maximum equivalent radius of $R_{max} = 2$ mm, at which time the pressure is raised to P_d. The considered bubble is located at an initial standoff $X = 1.5$ mm (i.e. $\bar{X} = 0.75$) from the material surface. It can be clearly seen in figure 21 that, with increasing amplitudes of the driving pressure, the bubble collapses with increasing speed.

Figure 22 shows the bubble shapes at the incompressible/compressible link moment for the same set of collapse driving pressures. It can be seen that in all cases, the

https://doi.org/10.1017/jfm.2014.394 Published online by Cambridge University Press

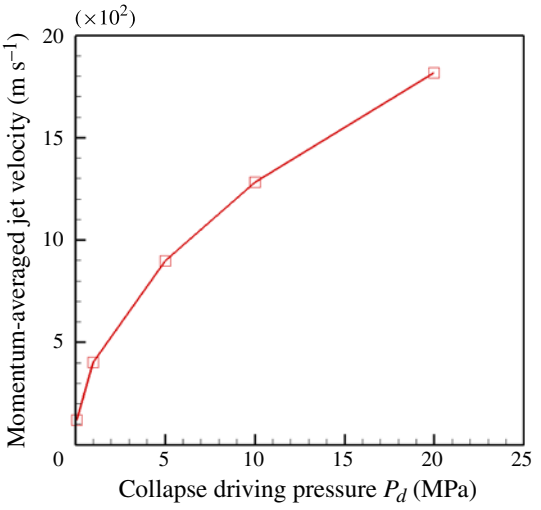


FIGURE 23. (Colour online) Variation of the re-entrant jet momentum-averaged velocity with the collapse driving pressure for $R_0 = 50$ μm, $R_{max} = 2$ mm, and $\bar{X} = 0.75$.

bubble shape is practically the same because the normalized standoff is the same. However, as seen in figure 21, the time at which the re-entrant jet reaches the other side of the bubble is very different between cases.

To quantitatively compare the effect of the driving pressure on the re-entrant jet behaviour we introduce as a jet characteristic the momentum-averaged jet velocity, $\boldsymbol{V}_{mom}$, defined as the average velocity in the whole re-entrant jet volume as follows:

$$\boldsymbol{V}_{mom} = \frac{1}{\mathscr{V}} \int \boldsymbol{V} \mathrm{d}\mathscr{V}, \tag{4.3}$$

where $\boldsymbol{V}$ is the liquid velocity at any point inside the jet, and $\mathscr{V}$ is the jet volume. As illustrated in figure 23 the computed momentum-averaged jet velocity at the touchdown moment is a strong function of P_d.

The pressure monitored at the plate centre for the different values of the collapse driving pressures is shown in figure 24. It is seen that the pressures peaks due to both the jet impact and the ring collapse increase as the collapse driving pressure, P_d, is increased. Furthermore, it is seen that the time lapse between the occurrences of these two pressure peaks becomes shorter as the collapse driving pressure is increased.

The effect of the collapse driving pressure on pit formation is shown in figure 25 for the two metallic alloys: aluminium Al7075 and stainless steel A2205. Once plastic deformation is reached, both the depth and the radius of the pit vary significantly with the collapse driving pressure, i.e. higher driving pressures result in deeper and wider pits. However, it is important to note that this cannot be extended beyond the material ultimate strength limit as failure modelling is not included.

4.3.2. *Effect of standoff between bubble and material*

This section describes the effect of bubble standoff on the formation of pits in the material. Figure 26 shows the time history of the bubble equivalent radius for different initial non-dimensional standoff distances: 0.5, 0.75, 1.0, and 1.5, while figure 27 shows the shape of the bubbles at a time close to the re-entrant jet touching the other

https://doi.org/10.1017/jfm.2014.394 Published online by Cambridge University Press

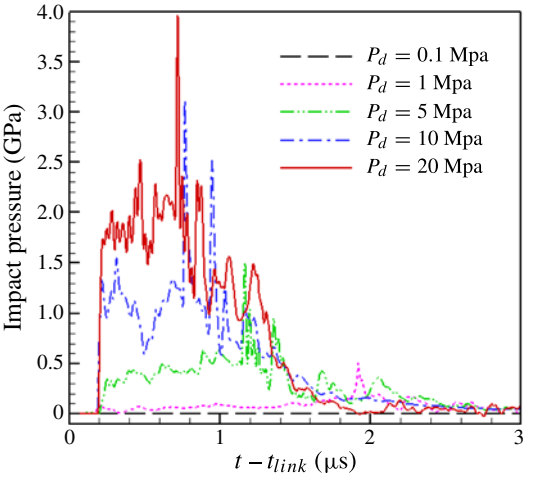


FIGURE 24. (Colour online) Time history of the pressure loading computed by the compressible code at the centre of the Al7075 plate top surface for different collapse driving pressures for $R_0 = 50$ μm, $R_{max} = 2$ mm and $\bar{X} = 0.75$.

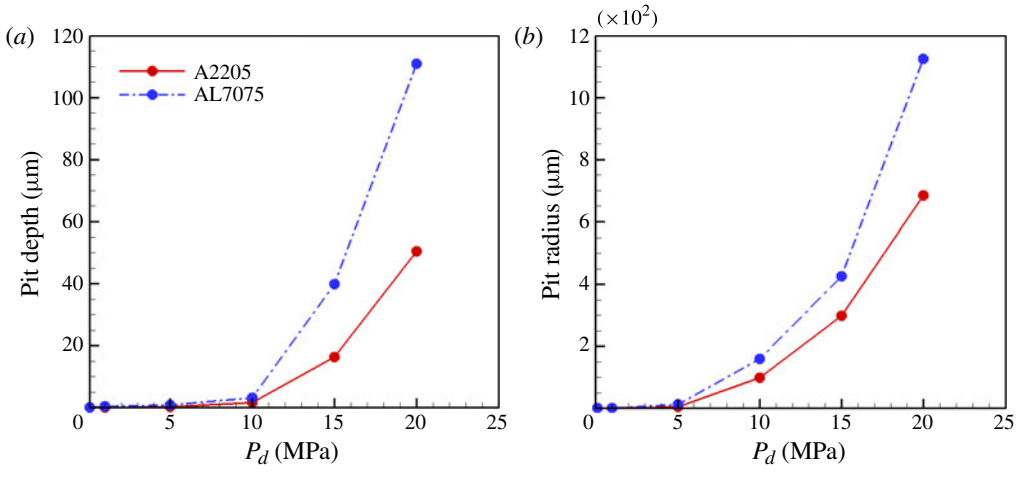


FIGURE 25. (Colour online) Comparison of (*a*) pit depth and (*b*) pit radius for Al7075 and A2205 for different collapse driving pressures for $R_0 = 50$ μm, $R_{max} = 2$ mm and $\bar{X} = 0.75$.

side of the bubble. Compressible flow computations were conducted after these points in time. In all cases shown, the bubble starts at $R_0 = 50$ μm, grows to a maximum $R_{max} = 2$ mm, and is then subjected to a pressure driving the collapse $P_d = 10$ MPa. The duration of the pressure drop, Δt, was adjusted such that the sudden pressure rise, P_d, was imposed at the time when the bubble radius reached 2 mm.

The bubble shapes show that the jet becomes more pronounced when the bubble is closer to the wall. At the larger standoffs, the bubble volume shrinks significantly before the jet develops, while closer to the wall the re-entrant jet develops much earlier and the bubble still has a larger volume when the jet reaches the opposite side of the bubbles. From these contours one can expect very different pressure loadings on the material surface for different values of X.

https://doi.org/10.1017/jfm.2014.394 Published online by Cambridge University Press

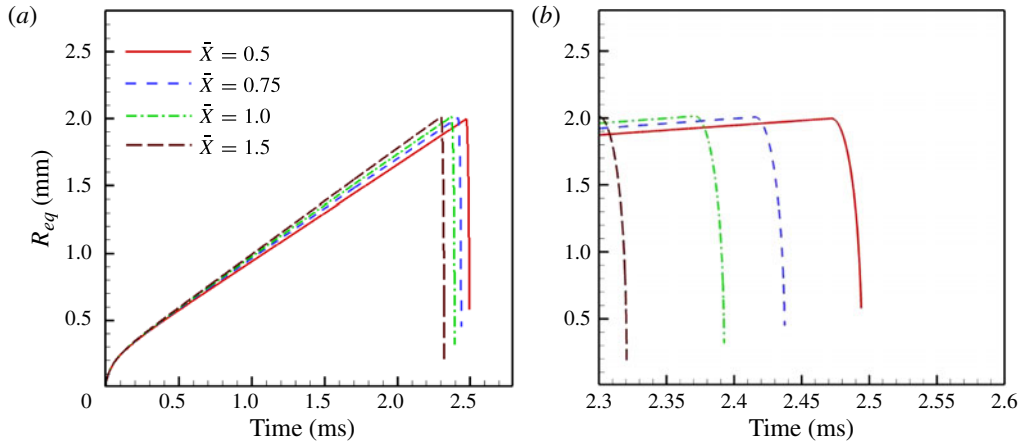


FIGURE 26. (Colour online) Evolution of the equivalent bubble radius for different standoff values at bubble maximum volume: (*a*) full history, (*b*) a zoom of the collapse phase.

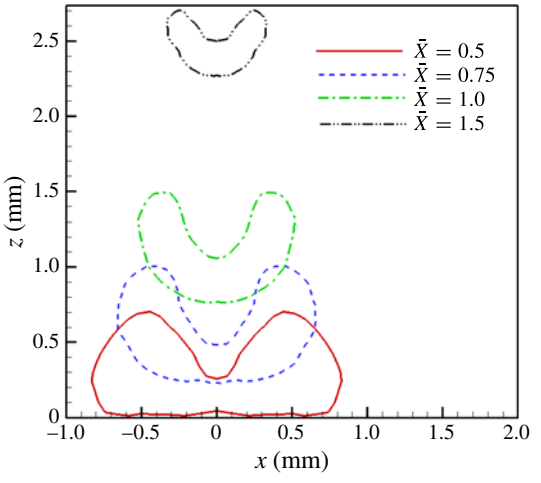


FIGURE 27. (Colour online) Bubble contours at the time of the compressible–incompressible link for different standoff distances between the bubble and the wall for $R_0 = 50$ μm, $R_{max} = 2$ mm and $P_d = 10$ MPa.

Figure 28(*a*) compares the momentum-averaged jet velocity, $\boldsymbol{V}_{mom}$, at the touchdown moment (time the jet reaches the other side of the bubble) for different standoff distances. It is seen that the jet velocity increases as the standoff distance is increased. This is not surprising since the largest bubble wall speed will actually be achieved when the bubble is spherical (Chahine *et al.* 2006; Jayaprakash *et al.*, 2013). A better illustration of the energy in the jet could be the total momentum of the jet, $\boldsymbol{V}_{mom}\mathscr{V}$, at the moment it touches the opposite side of the bubble, which is shown in figure 28(*b*).

Here we can see that there is an optimum distance ($\bar{X} \sim 0.75$) at which the energy in the jet is maximal. Similar observations have been reported in both numerical studies (Chahine *et al.* 1996; Jayaprakash *et al.* 2012) and experimental studies (Philipp &

https://doi.org/10.1017/jfm.2014.394 Published online by Cambridge University Press

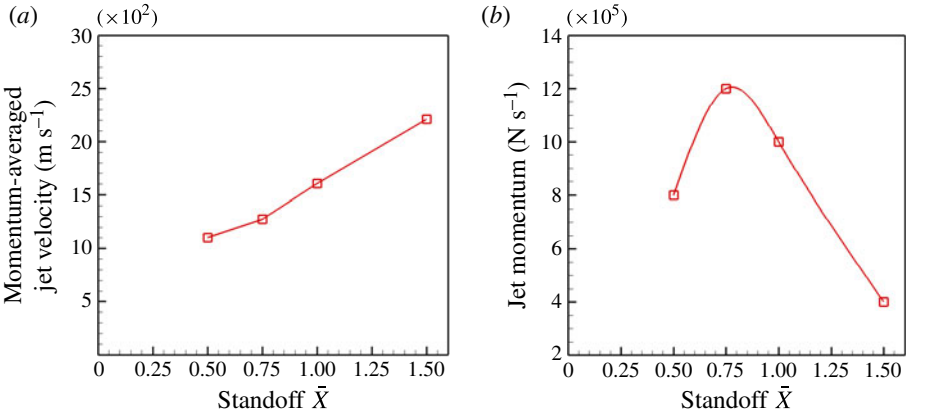


FIGURE 28. (Colour online) Variations with the bubble–wall standoff distance of (*a*) $\boldsymbol{V}_{mom}$, the momentum-averaged jet velocity, and (*b*) the jet momentum at touchdown, for $R_0 = 50$ μm, $R_{max} = 2$ mm and $P_d = 10$ MPa.

Lauterborn 1998; Vogel & Lauterborn 1988; Harris *et al.* 2009). Actually, a higher jet velocity does not necessarily result in a higher impact pressure on the wall because the distance between the jet front and the wall at the touchdown moment is also very important. This is illustrated in the material deformation results.

Figure 29 shows the pressure versus time monitored at the plate centre for different standoff distances. It is seen that the pressure loading due to the jet impact is much higher for smaller standoff, especially for $\bar{X} = 0.5$, since in this case the re-entrant jet directly impacts on the material surface when it penetrates the other side of the bubble. As the standoff increases, the magnitude of the pressure due to the jet impact is reduced because the high-speed liquid has to travel a longer distance while submerged before reaching the material surface. For $\bar{X} = 1.5$, only one significant pressure peak with a typical exponential decay is observed because the jet touchdown occurs almost at the same time as when the bubble reaches the minimum size and no jet reaches the wall. Instead, a shock-wave-type pressure profile is observed.

The effect of the bubble–material standoff distance on the pit characteristics is in fact the most important and relevant piece of information for damage assessment. Figures 30(*a*), 30(*b*) and 30(*c*) show the pit characteristics for the two metallic alloys studied: depth, radius, and volume respectively as a function of the normalized standoff distance. Figure 30(*a,c*) shows that pit depth and volume continually decrease when the standoff distance increases. However, like the jet momentum, pit radius goes through a maximum when the standoff distance is close to $\bar{X} = 0.75$. The volume, not provided directly by the software, was approximated by the volume of a cone with the same base diameter and height. In fact, the shape of the pit varies with standoff as shown in figure 31. At the smallest standoffs, the pit radius is smaller with $\bar{X} = 0.5$ than with $\bar{X} = 0.75$, while the pit depth is larger with $\bar{X} = 0.5$ than with $\bar{X} = 0.75$.

4.3.3. *Effect of maximum bubble size*

This section describes the effect of the maximum bubble size, R_{max}, on the characteristics of the material pits formed in response to cavitation bubble collapse. For this study the duration of the pressure drop, Δt, in (4.1) was adjusted to obtain

https://doi.org/10.1017/jfm.2014.394 Published online by Cambridge University Press

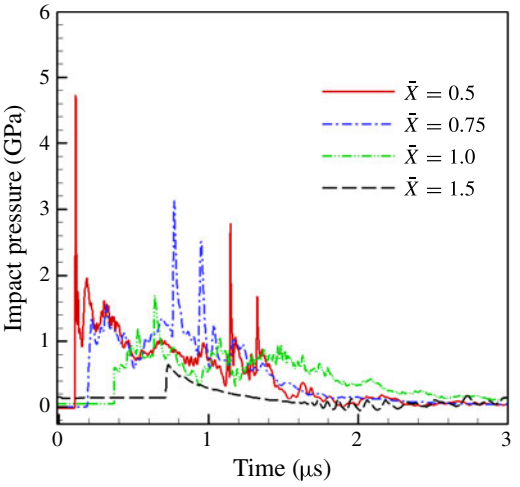


FIGURE 29. (Colour online) Pressure versus time at the centre of the Al7075 plate for different bubble–plate standoff distances for $R_0 = 50$ μm, $R_{max} = 2$ mm and $P_d = 10$ MPa.

the desired R_{max}. The shapes of the bubbles close to re-entrant jet touching the other side of the bubble for the different R_{max}(0.5, 1.0, 1.5 and 2.0 mm) are shown in figure 32. These shapes indicate that the moment of jet touchdown on the opposite side of the bubble occurs closer to the moment when the jet impacts the wall as R_{max} decreases. However, the volume and thus the momentum in the jet varies in the opposite direction, i.e. the bubble volume and the momentum at collapse are smaller for smaller R_{max}.

The momentum-averaged jet velocity, $\boldsymbol{V}_{mom}$, and the jet momentum, $\boldsymbol{V}_{mom}\mathscr{V}$, at the touchdown moment for different R_{max} are shown in figure 33. It is seen that the jet velocity is almost independent of the value of R_{max} even though the time of jet impact decreases as R_{max} is decreased. The momentum is therefore more dependent on the jet volume and increases with R_{max} and it is expected that damage will simply increase also with R_{max}.

Figure 34 shows the pressure monitored at the plate centre for different standoff distances. For all cases, the initial pressure peak due the jet impact and the second peak due to bubble ring collapse are observed and they both increase as R_{max} is increased. It is also seen that the time lapse between the occurrences of these two pressure peaks becomes longer and results in a higher impulse as R_{max} is increased. This implies that the jet momentum at touchdown has a better correlation with the pressure loading on the material surface.

The effect of the R_{max} on pit formation is shown in figures 35(*a*) and 35(*b*) by comparing the pit characteristics, depth and radius respectively, for the two metallic alloys studied. Both pit depth and pit radius are seen to increase as R_{max} is increased as expected from the observations in the previous figures. The relationship between the pit dimensions and the bubble radius is practically linear.

4.3.4. *Effect of material type*

In addition to the two metallic alloys considered above, three compliant materials with the properties described in § 2.5 were also studied for their response to the cavitation-bubble pressure loading. Due to the low compressive and shear strength of

https://doi.org/10.1017/jfm.2014.394 Published online by Cambridge University Press

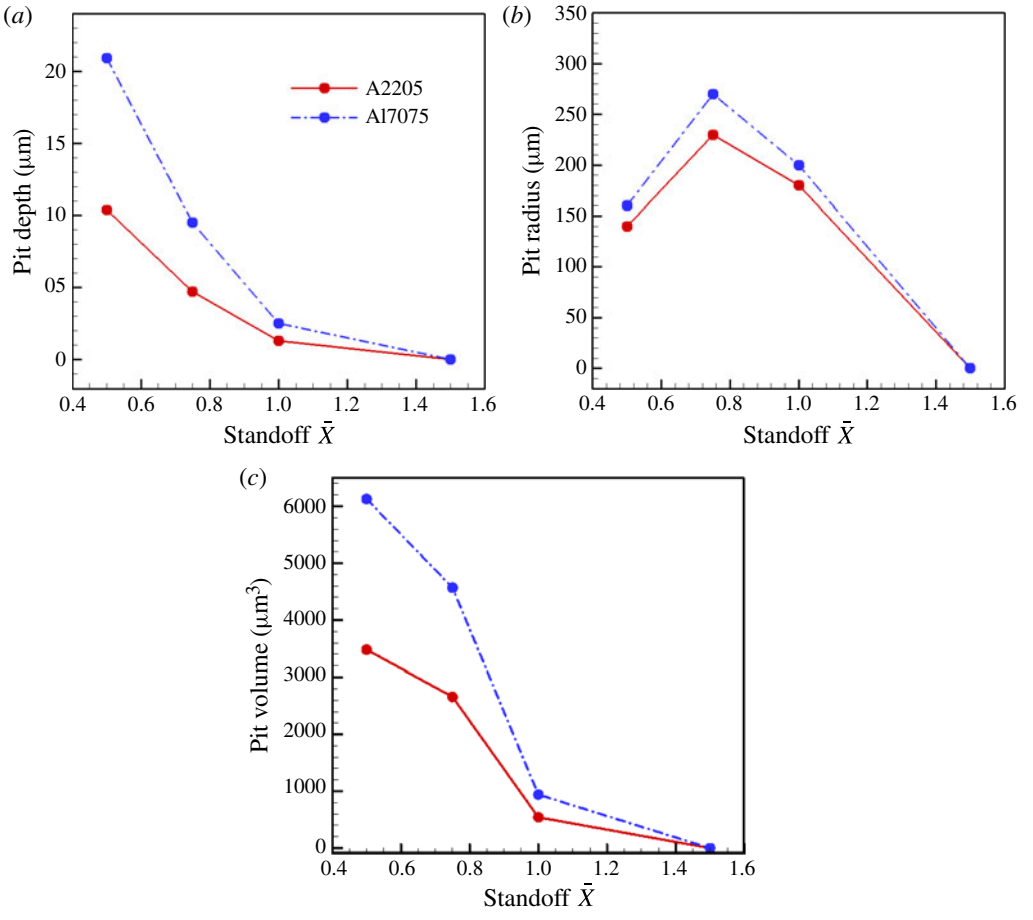


FIGURE 30. (Colour online) Variation of (*a*) pit depth, (*b*) pit radius and (*c*) pit volume with the normalized standoff distance for Al7075 and A2205 for $R_0 = 50$ μm, $R_{max} = 2$ mm and $P_d = 10$ MPa.

the compliant materials considered, a smaller collapse driving pressure, $P_d = 0.1$ MPa, was chosen to avoid numerical issues caused by over-squeezed elements with the large P_d used with the metallic allows. The other conditions for the bubble dynamics presented for the base case were maintained.

Figure 36 shows the impact pressure recorded at the plate centre for this collapse driving pressure. Also included in figure 36 for comparison are the time histories of the pressures on the two metallic alloys and on a rigid fixed plate. The figure shows that the impact pressures for the metallic alloys and the rigid plate are very close. On the other hand, on the compliant materials, due to absorption through deformation of some of the energy, lower magnitudes of the impact pressures are seen. This has already been observed experimentally by Chahine & Kalumuck (1998*b*). Also, a delay in the peak timing occurs because of the modification of the bubble dynamics by the compliant surface.

Since the selected collapse driving pressure was small, no permanent deformation was observed in the metallic alloys. In addition, the chosen viscoelastic properties of the compliant materials do not allow for permanent deformation. Therefore, to

https://doi.org/10.1017/jfm.2014.394 Published online by Cambridge University Press

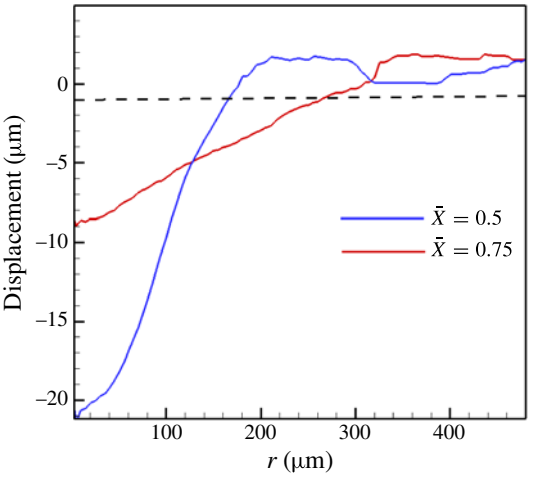


FIGURE 31. (Colour online) Comparison of pit shape between $\bar{X} = 0.5$ and $\bar{X} = 0.75$ for Al7075 for $R_0 = 50$ μm, $R_{max} = 2$ mm and $P_d = 10$ MPa.

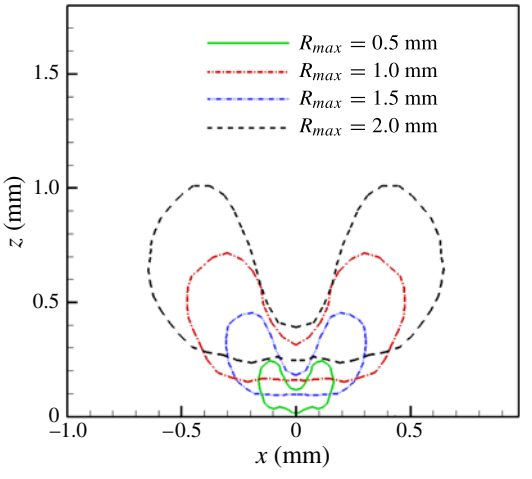


FIGURE 32. (Colour online) Bubble contours at the compressible–incompressible link for different maximum bubble size for $R_0 = 50$ μm, $P_d = 10$ MPa and $\bar{X} = 0.75$.

study the dynamics, we compare the maximum depth achieved during the dynamics in each case. Figure 37 shows a comparison of the maximum time-dependent displacement of the plate surface centre recorded for the two metallic alloys and for the three compliant materials. Loadings for two bubble-collapse driving pressures are considered. As expected, the stainless steel, A2205, shows the smallest depth value, while of the compliant materials, rubber 2 (polyurethane) shows the maximum deformation.

5. Conclusions

Material pitting due to cavitation bubble collapse is studied by modelling the dynamics of growing and collapsing cavitation bubbles near a deforming material

https://doi.org/10.1017/jfm.2014.394 Published online by Cambridge University Press

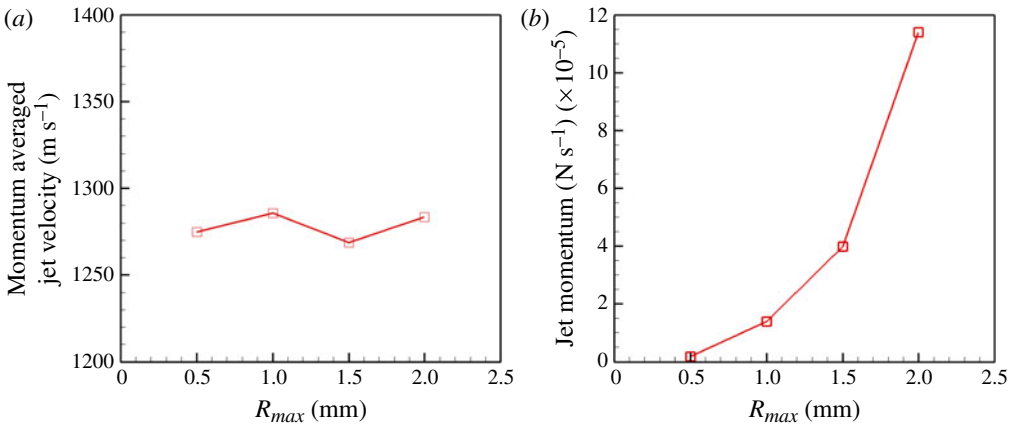


FIGURE 33. (Colour online) Variation with R_{max} of (*a*) momentum-averaged jet velocity, $\boldsymbol{V}_{mom}$, and (*b*) jet momentum at touchdown, $\boldsymbol{V}_{mom}\mathscr{V}$, for $R_0 = 50$ μm, $P_d = 10$ MPa and $\bar{X} = 0.75$.

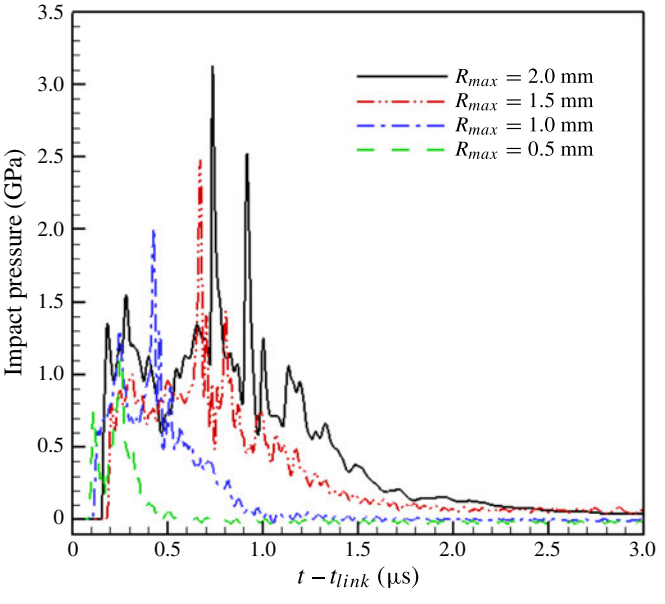


FIGURE 34. (Colour online) Pressure versus time at the centre of the Al7075 plate for different values of the maximum bubble radius for $R_0 = 50$ μm, $P_d = 10$ MPa and $\bar{X} = 0.75$.

with an initially flat surface. The bubble nucleus, initially at equilibrium with the surrounding liquid near the wall, is subjected to a time-dependent pressure field. The pressure first drops to a value below the bubble critical pressure, stays at this pressure for a prescribed time, and then rises to a high value. The nucleus then grows explosively and collapses violently near the wall forming a fast re-entrant jet, which hits the wall and deforms it permanently when the collapse intensity is high enough to result in stresses exceeding the material elastic limit.

https://doi.org/10.1017/jfm.2014.394 Published online by Cambridge University Press

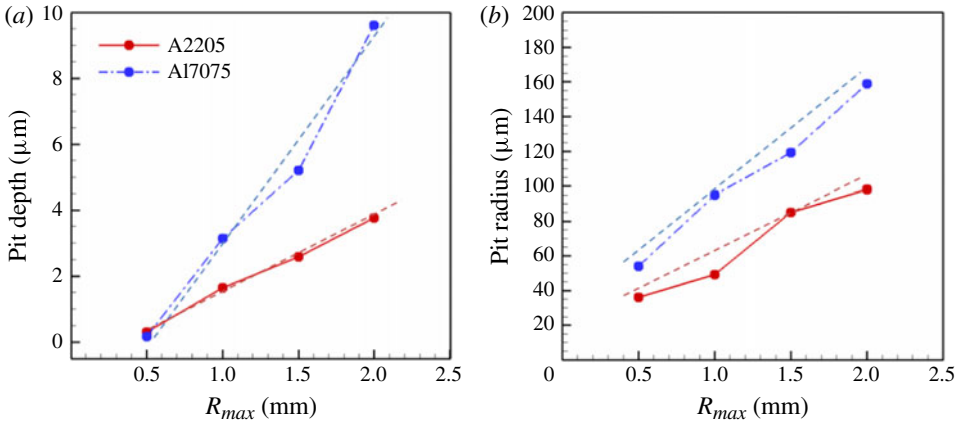


FIGURE 35. (Colour online) Comparison of (*a*) pit depth and (*b*) pit radius between Al7075 and A2205 for cases with different values of R_{max} for $R_0 = 50$ μm, $P_d = 10$ MPa and $\bar{X} = 0.75$.

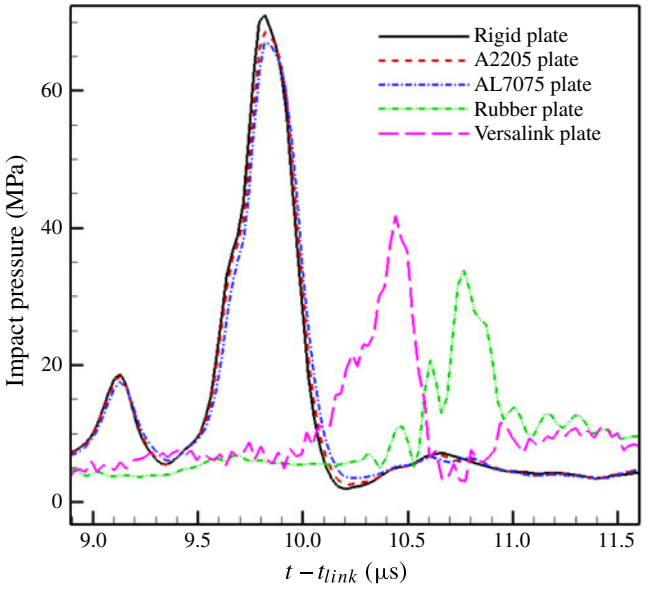


FIGURE 36. (Colour online) Time history of the pressure at the plate centre for two metallic alloys, a rigid wall, and two compliant materials for $R_0 = 50$ μm, $R_{max} = 2$ mm, $P_d = 0.1$ MPa and $\bar{X} = 0.75$.

The pressure loading on the material surface during the bubble collapse is found to be due to the re-entrant jet impact and to the collapse of the remaining bubble ring. The magnitude of the pressure peaks felt by the material depends on the response and amount of deformation of the solid. The FSI simulations show that the load on the material is reduced and this reduction increases when the solid boundary deformation increases and more energy is absorbed. For the conditions studied in this paper, during bubble growth and dynamics till the re-entrant jet impact, material

https://doi.org/10.1017/jfm.2014.394 Published online by Cambridge University Press

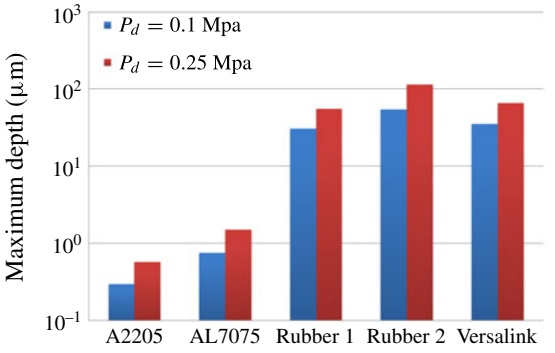


FIGURE 37. (Colour online) Comparison of the maximum plate centre vertical displacement for metallic and compliant materials in response to bubble loading at two collapse driving pressures, $P_d = 0.1$ and 0.25 MPa.

deformations remain negligible compared to the later material deformations resulting from bubble re-entrant jet impact and bubble ring collapse.

The high-pressure loading results in high-stress waves, which propagate radially from the loading location into the material and cause the deformation. A pit (permanent deformation) is formed when the local equivalent stresses exceed the material yield stress.

The loading is highly dependent on the amplitude of the pressure which drives the bubble collapse, the standoff distance, and the duration of the depressurization. The parametric investigation conducted in this study shows that the pressure peaks due to both the jet impact and the ring collapse increase as the collapse driving pressure is increased, and the time lapse between the occurrences of these two pressure peaks becomes shorter as the collapse driving pressure is increased. Also, higher collapse driving pressures cause the bubble to collapse faster and result in higher pressure loadings on the materials and deeper and wider pits.

The initial standoff distance between the bubble and the material affects the jet characteristics in a non-monotonic fashion. Higher jet velocities occur at the larger standoff distances. However, the energy in the jet is maximum at a normalized standoff distance close to $\bar{X} = 0.75$. A higher jet velocity does not necessarily result in a higher impact pressure, since the impact pressure also depends on the distance between the wall and the jet front at the touchdown moment. A more concentrated pressure loading on the material surface is obtained for smaller standoffs where the jet touches downs and the bubble ring collapses very close to the wall. Such concentrated pressure loadings result in deeper but narrower pits. As a result, the shape of the pit, i.e. the ratio of pit radius and depth, does not vary monotonically with standoff.

The maximum bubble size does not have a significant effect on the jet velocity. However, it significantly affects the momentum in the jet as it influences a larger material surface area. This results in deeper and wider pits for larger bubble sizes.

From the study of different material types, it was found that material response has a strong effect on the impact pressures due to strong FSI. Impact pressures for metallic alloys are very close to those on a rigid plate while compliant materials deform and absorb energy. This results in lower magnitude of the impact pressures and delays in peak occurrence due to lengthening of the bubble period.

https://doi.org/10.1017/jfm.2014.394 Published online by Cambridge University Press

Acknowledgements

This work was conducted under partial support from Dynaflow, Inc. internal IR&D and from the Office of Naval Research under Contract N00014-12-M-0238, monitored by Dr K.-H. Kim. We would also like to thank ONR and G. Harris from the Naval Surface Warfare Center, Indian Head, for allowing us access to the GEMINI code and contribution to its coupling to the DYNA3D Structure code. Their support is greatly appreciated.

REFERENCES

AMIRKHIZI, A. V., ISAACS, J., MCGEE, J. & NEMAT-NASSER, S. 2006 An experimentally-based viscoelastic constitutive model for polyurea, including pressure and temperature effects. *Phil. Mag.* **86** (36), 5847–5866.

ANDERSON, J. D. 1990 *Modern Compressible Flow: with Historical Perspective,* vol. 12. McGraw-Hill.

BLAKE, J. R. & GIBSON, D. C. 1987 Cavitation bubbles near boundaries. *Annu. Rev. Fluid Mech.* **19**, 99–124.

BRENNEN, C. E. 1995 *Cavitation and Bubble Dynamics*. Oxford University Press.

CHAHINE, G. L. 1982 Experimental and asymptotic study of non-spherical bubble collapse. *Appl. Sci. Res.* **38**, 187–197.

CHAHINE, G. L. 1993 Cavitation dynamics at microscale level. *J. Heart Valve Dis.* **3**, 102–116.

CHAHINE, G. L. 2014 Modeling of cavitation dynamics and interaction with material. In *Advanced Experimental and Numerical Techniques for Cavitation Erosion Prediction* (ed. K. H. Kim, G. L. Chahine, J. P. Franc & A. Karimi), chap. 6. Springer.

CHAHINE, G. L., ANNASAMI, R., HSIAO, C.-T. & HARRIS, G. 2006 Scaling rules for the prediction on UNDEX bubble re-entering jet parameters. *SAVIAC Crit. Technol. Shock Vib.* **4** (1), 1–12.

CHAHINE, G. L., DURAISWAMI, R. & KALUMUCK, K. M. 1996 Boundary element method for calculating 2-D and 3-D underwater explosion bubble loading on nearby structures. *Report* NSWCDD/TR-93/46. Naval Surface Warfare Center, Weapons Research and Technology Department, September (limited distribution).

CHAHINE, G. L. & KALUMUCK, K. M. 1998*a* BEM software for free surface flow simulation including fluid structure interaction effects. *Intl J. Comput. Appl. Technol.* **11** (3/4/5), 177–199.

CHAHINE, G. L. & KALUMUCK, K. M. 1998*b* The influence of structural deformation on water jet impact loading. *J. Fluids Struct.* **12** (1), 103–121.

CHAHINE, G. L. & PERDUE, T. O. 1990 Simulation of the three-dimensional behavior of an unsteady large bubble near a structure. In *3rd International Colloquium on Drops and Bubbles, Monterey, CA*, AIP Conf. Proc., vol. 197, p. 188.

CHAHINE, G. L. & SHEN, Y. T. 1986 Bubble dynamics and cavitation inception in cavitation susceptibility meter. *Trans. ASME: J. Fluids Engng* **108**, 444–452.

COLELLA, P. 1985 A direct Eulerian MUSCL scheme for gas dynamics. *SIAM J. Sci. Stat. Comput.* **6** (1), 104–117.

CRUM, L. A. 1979 Surface oscillations and jet development in pulsating bubbles. *J. Phys. Paris* **40** (supplément au N. 11), c8-285 colloque c8.

DUNCAN, J. H., MILLIGAN, C. D. & ZHANGE, S. 1991 On the interaction of a collapsing cavity and a compilant wall. *J. Fluid Mech.* **226**, 401–423.

DUNCAN, J. H., MILLIGAN, C. D. & ZHANG, S. 1996 On the interaction between a bubble and submerged compliant structure. *J. Sound Vib.* **197**, 17–44.

HARRIS, G. S., ILLAMNI, R., LEWIS, W., RYE, K. & CHAHINE, G. L. 2009 Underwater explosion bubble phenomena tests near a simulated dam structure. *IHTR* 10-3055, November 1. Naval Surface Warfare Center – Indian Head Division.

HSIAO, C.-T. & CHAHINE, G. L. 2013*a* Development of compressible–incompressible link to efficiently model bubble dynamics near floating body. *Adv. Bound. Element Meshless Tech.* **XIV**, 141–152.

https://doi.org/10.1017/jfm.2014.394 Published online by Cambridge University Press

HSIAO, C.-T. & CHAHINE, G. L. 2013*b* Breakup of finite thickness viscous shell microbubbles by ultrasound: a simplified zero thickness shell model. *J. Acoust. Soc. Am.* **133** (4), 1897–1910.

JAYAPRAKASH, A., HSIAO, C.-T. & CHAHINE, G. L. 2012 Numerical and experimental study of the interaction of a spark-generated bubble and a vertical wall. *Trans. ASME: J. Fluids Engng* **134**, 031301.

JONES, I. R. & EDWARDS, D. H. 1960 An experimental study of the forces generated by the collapse of transient cavities in water. *J. Fluid Mech.* **7**, 596–609.

KALUMUCK, K. M., CHAHINE, G. L. & HSIAO, C.-T. 2003 Simulation of surface piercing body coupled response to underwater bubble dynamics utilizing 3DYNAFS©, a three-dimensional BEM code. *Comput. Mech.* **32**, 319–326.

KALUMUCK, K. M., DURAISWAMI, R. & CHAHINE, G. L. 1995 Bubble dynamics fluid–structure interaction simulation on coupling fluid BEM and structural FEM codes. *J. Fluids Struct.* **9**, 861–883.

KAPAHI, A., HSIAO, C.-T. & CHAHINE, G. L. 2014 A multi-material flow solver for high speed compressible flow applications. *Comput. Fluids* (in press).

KEY, S. W. 1974 HONDO-a finite element computer program for the large deformation dynamics response of axisymmetric solids. *Report* 74-0039. Sandia National Laboratories, Albuquerque, NM.

KIM, K. H., CHAHINE, G. L., FRANC, J. P. & KARIMI, A. 2014 *Advanced Experimental and Numerical Techniques for Cavitation Erosion Prediction*. Springer.

MADADI-KANDJANI, E. & XIONG, Q. 2014 Validity of the spring-backed membrane model for bubble-wall interactions with compliant walls. *Comput. Fluids* **96**, 116–121.

NAUDE, C. F. & ELLIS, A. T. 1961 On the mechanism of cavitation damage by non-hemispherical cavities collapsing in contact with a solid boundary. *Trans. ASME: J. Basic Engng* **83**, 648–656.

PHILIPP, A. & LAUTERBORN, W. 1998 Cavitation erosion by single laser-produced bubbles. *J. Fluid Mech.* **361**, 75–116.

PLESSET, M. S. & CHAPMAN, R. B. 1971 Collapse of an initially spherical vapour cavity in the neighborhood of a solid boundary. *J. Fluid Mech.* **47** (2), 283–290.

RAYLEIGH, LORD 1917 On the pressure developed in a liquid during the collapse of a spherical cavity. *Phil. Mag.* **34**, 94–98.

VOGEL, A. & LAUTERBORN, W. 1988 Acoustic transient generation by laser-produced cavitation bubbles near solid boundaries. *J. Acoust. Soc. Am.* **84**, 719–731.

WANG, Q. X. 2013 Underwater explosion bubble dynamics in a compressible liquid. *Phys. Fluids* **25**, 072104.

WANG, Q. X. & BLAKE, J. R. 2010 Non-spherical bubble dynamics in a compressible liquid. Part 1. Travelling acoustic wave. *J. Fluid Mech.* **659**, 191–224.

WANG, Q. X. & BLAKE, J. R. 2011 Non-spherical bubble dynamics in a compressible liquid. Part 2. Acoustic standing wave. *J. Fluid Mech.* **679**, 559–581.

WARDLAW, A. B. JR. & LUTON, A. J. 2000 Fluid structure interaction for close-in explosion. *Shock Vib.* **7**, 265–275.

WARDLAW, A. B., LUTON, J. A., RENZI, J. R., KIDDY, K. C. & MCKEOWN, R. M. 2003 The Gemini Euler solver for the coupled simulation of underwater explosions. *Tech. Rep.* 2500, November. Naval Surface Warfare Center – Indian Head Division.

WHIRLEY, R. G. & ENGELMANN, B. E. 1993 DYNA3D: a nonlinear, explicit, three-dimensional finite element code for solid and structural mechanics – user manual. *Rep.* UCRL-MA-107254 Rev. 1. Lawrence Livermore National Laboratory, November.

ZEL'DOVICH, Y. B. & RAIZER, Y. P. 2002 *Physics of Shock Waves and High-Temperature Hydrodynamic Phenomena*. Dover.

ZHANG, S., DUNCAN, J. H. & CHAHINE, G. L. 1993 The final stage of the collapse of a cavitation bubble near a rigid wall. *J. Fluid Mech.* **257**, 147–181.

https://doi.org/10.1017/jfm.2014.394 Published online by Cambridge University Press